



An efficient and accurate two-stage fourth-order gas-kinetic scheme for the Euler and Navier–Stokes equations



Liang Pan^a, Kun Xu^{b,c,*}, Qibing Li^d, Jiequan Li^a

^a Institute of Applied Physics and Computational Mathematics, Beijing, 100088, China

^b Department of Mathematics, Hong Kong University of Science and Technology, Clear Water Bay, Kowloon, Hong Kong

^c Department of Mechanical and Aerospace Engineering, Hong Kong University of Science and Technology, Clear Water Bay, Kowloon, Hong Kong

^d School of Aerospace, Tsinghua University, Beijing 100084, China

ARTICLE INFO

Article history:

Received 18 February 2016

Received in revised form 7 June 2016

Accepted 31 August 2016

Available online 6 September 2016

Keywords:

Two-stage Lax–Wendroff-type time stepping method

Fourth-order gas-kinetic scheme

Navier–Stokes equations

ABSTRACT

For computational fluid dynamics (CFD), the generalized Riemann problem (GRP) solver and the second-order gas-kinetic scheme (GKS) provide a time-accurate flux function starting from a discontinuous piecewise linear flow distributions around a cell interface. With the adoption of time derivative of the flux function, a two-stage Lax–Wendroff-type (L-W for short) time stepping method has been recently proposed in the design of a fourth-order time accurate method for inviscid flow [21]. In this paper, based on the same time-stepping method and the second-order GKS flux function [42], a fourth-order gas-kinetic scheme is constructed for the Euler and Navier–Stokes (NS) equations. In comparison with the formal one-stage time-stepping third-order gas-kinetic solver [24], the current fourth-order method not only reduces the complexity of the flux function, but also improves the accuracy of the scheme. In terms of the computational cost, a two-dimensional third-order GKS flux function takes about six times of the computational time of a second-order GKS flux function. However, a fifth-order WENO reconstruction may take more than ten times of the computational cost of a second-order GKS flux function. Therefore, it is fully legitimate to develop a two-stage fourth order time accurate method (two reconstruction) instead of standard four stage fourth-order Runge–Kutta method (four reconstruction). Most importantly, the robustness of the fourth-order GKS is as good as the second-order one. In the current computational fluid dynamics (CFD) research, it is still a difficult problem to extend the higher-order Euler solver to the NS one due to the change of governing equations from hyperbolic to parabolic type and the initial interface discontinuity. This problem remains distinctively for the hypersonic viscous and heat conducting flow. The GKS is based on the kinetic equation with the hyperbolic transport and the relaxation source term. The time-dependent GKS flux function provides a dynamic process of evolution from the kinetic scale particle free transport to the hydrodynamic scale wave propagation, which provides the physics for the non-equilibrium numerical shock structure construction to the near equilibrium NS solution. As a result, with the implementation of the fifth-order WENO initial reconstruction, in the smooth region the current two-stage GKS provides an accuracy of $\mathcal{O}((\Delta x)^5, (\Delta t)^4)$ for the Euler equations, and $\mathcal{O}((\Delta x)^5, \tau^2 \Delta t)$ for the NS equations, where τ is the time between particle collisions. Many numerical tests, including difficult ones for the Navier–Stokes solvers, have been used to validate the current method. Perfect numerical solutions can be obtained from the high Reynolds number boundary layer to the hypersonic viscous heat conducting flow. Following the two-stage time-stepping framework, the third-order GKS flux function can be used as

* Corresponding author at: Department of Mathematics, Hong Kong University of Science and Technology, Clear Water Bay, Kowloon, Hong Kong.
E-mail addresses: panliangju@sina.com (L. Pan), makxu@ust.hk (K. Xu), lbq@tsinghua.edu.cn (Q. Li), li_jiequan@iapcm.ac.cn (J. Li).

well to construct a fifth-order method with the usage of both first-order and second-order time derivatives of the flux function. The use of time-accurate flux function may have great advantages on the development of higher-order CFD methods.

© 2016 Elsevier Inc. All rights reserved.

1. Introduction

To develop third and higher-order numerical methods has attracted great attention in recent decades. In comparison with second-order schemes, which were mostly developed in the 70s and 80s, the higher-order methods can provide more accurate solutions, but they are less robust and more complicated. There are many review papers and monographs about the current status of higher-order schemes, which include the discontinuous Galerkin (DG) [7], essential non-oscillatory (ENO) [13], weighted essential non-oscillatory (WENO) [27], $P_N P_M$ [9], multi-moment constrained method [14], and many others. Most of those methods use the Runge–Kutta time-stepping approach to achieve higher order temporal accuracy [11]. Based on the time-independent flux function of the Riemann solver [36], in order to achieve a fourth-order time accuracy, a four-stage Runge–Kutta time stepping method is usually used. Sometimes, the CFL number for higher-order methods strongly depends on the order of the scheme, such as the DG method. For the WENO-type schemes, the initial reconstruction may take a significant amount of computational time in comparison with the computational cost of the flux function, especially for the multiple reconstructions in the Runge–Kutta method. For the same accuracy, any possible reduction of middle stages in the Runge–Kutta method will be important for the improvement of the efficiency of the scheme.

Recently, based on the time-dependent flux function of the generalized Riemann problem (GRP) [1–3], a two-stage fourth order time-accurate discretization was developed for Lax–Wendroff type (L-W for short) flow solvers, particularly applied for the hyperbolic conservation laws [21]. The reason for the success of a two-stage L-W type time stepping method in achieving a fourth-order time accuracy is solely due to the use of both flux function and its time derivative. In terms of the gas evolution model, the gas-kinetic scheme (GKS) provides a time accurate flux function as well, even though it depends on time through a much more complicated relaxation process from the kinetic to the hydrodynamic scale physics than the time-dependent flux function of GRP for the inviscid flow. The return for such a flux function is that the viscous and heat conducting terms can be recovered as well. This paper is about the construction of a fourth-order time accurate gas-kinetic scheme (GKS) with the two-stage temporal discretization for the Euler and Navier–Stokes (NS) equations.

For the Euler and NS solutions, second-order and third-order gas-kinetic schemes have been constructed in the past years [42,24,18,33]. The flux evaluation in the scheme is based on the time evolution of flow variables from an initial piece-wise discontinuous polynomials around a cell interface, where high-order spatial and temporal evolutions of a gas distribution function are coupled nonlinearly. In comparison with other high-order schemes, the GKS integrates the flux function over a time step analytically without employing the multi-stage Runge–Kutta time stepping techniques. So, in terms of third-order GKS [28], it may not become expensive in comparison with other schemes with Runge–Kutta time stepping, because the WENO-type reconstruction is much more expensive than the third-order flux function. Different from the CFD methods based on the macroscopic governing equations, the main advantages of the GKS are the followings. (i) The inviscid and viscous coupling in the flux evolution [42]; (ii) Multi-dimensionality with the inclusion of both normal and tangential gradients of flow variables in the flux evaluation across a cell interface [45]; (iii) Compact stencils can be constructed with the use of both cell averaged and cell interface flow variables at the next time level [30]; (iv) Extension to the whole flow regime from rarefied to the continuum one [43]. However, with the one-stage gas evolution model, the formulation of GKS can become very complicated for the further improvement of the order of the scheme, such as to the fourth-order method [26], especially for multidimensional computation. The two-stage L-W time stepping method in [21] provides an alternative framework for the development of a fourth-order GKS with a second-order flux function. In this paper, we are going to present such a fourth-order GKS for the Euler and Navier–Stokes solutions. The current scheme can use a time step with CFL number on the order of 0.5. Most importantly, the current fourth-order GKS is as robust as the second-order method, which works perfectly from the subsonic to the hypersonic viscous heat conducting flows. The numerical accuracy of the scheme will be analyzed. As a further extension, the third-order GKS flux function [32,24,28] can be also used to construct two-stage fifth-order temporal accurate methods with the inclusion of both first-order and second-order time derivatives of the flux function. The detailed formulation is presented in the Appendix of this paper. Theoretically, this process for constructing even higher-order schemes can go forward continuously.

This paper is organized as follows. In Section 2, the general formulation for the two-stage temporal discretization is introduced. In Section 3, a fourth-order gas-kinetic scheme is presented based on the two-stage time discretization. Section 4 includes numerical examples to validate the current algorithm. The last section is the conclusion. The extension for the construction of two-stage fifth-order scheme is given in Appendix.

2. Fourth-order temporal discretization

A two-stage fourth-order time-accurate discretization was developed for Lax–Wendroff flow solvers, particularly applied for hyperbolic equations with the generalized Riemann problem (GRP) solver [21]. Consider the following time-dependent equation,

$$\frac{\partial \mathbf{w}}{\partial t} = \mathcal{L}(\mathbf{w}), \quad (1)$$

with the initial condition at t_n , i.e.,

$$\mathbf{w}(t = t_n) = \mathbf{w}^n, \quad (2)$$

where \mathcal{L} is an operator for spatial derivative of flux. The time derivatives are obtained using the Cauchy–Kovalevskaya method,

$$\frac{\partial \mathbf{w}^n}{\partial t} = \mathcal{L}(\mathbf{w}^n), \quad \frac{\partial}{\partial t} \mathcal{L}(\mathbf{w}^n) = \frac{\partial}{\partial \mathbf{w}} \mathcal{L}(\mathbf{w}^n) \mathcal{L}(\mathbf{w}^n).$$

Introducing an intermediate state at $t^* = t_n + \Delta t/2$,

$$\mathbf{w}^* = \mathbf{w}^n + \frac{1}{2} \Delta t \mathcal{L}(\mathbf{w}^n) + \frac{1}{8} \Delta t^2 \frac{\partial}{\partial t} \mathcal{L}(\mathbf{w}^n), \quad (3)$$

the corresponding time derivatives are obtained as well for the intermediate state,

$$\frac{\partial \mathbf{w}^*}{\partial t} = \mathcal{L}(\mathbf{w}^*), \quad \frac{\partial}{\partial t} \mathcal{L}(\mathbf{w}^*) = \frac{\partial}{\partial \mathbf{w}} \mathcal{L}(\mathbf{w}^*) \mathcal{L}(\mathbf{w}^*).$$

Then, the state \mathbf{w} can be updated with the following formula,

$$\mathbf{w}^{n+1} = \mathbf{w}^n + \Delta t \mathcal{L}(\mathbf{w}^n) + \frac{1}{6} \Delta t^2 \left(\frac{\partial}{\partial t} \mathcal{L}(\mathbf{w}^n) + 2 \frac{\partial}{\partial t} \mathcal{L}(\mathbf{w}^*) \right). \quad (4)$$

It can be proved that for hyperbolic equations the above time stepping method Eq. (4) provides a fourth-order time accurate solution for $\mathbf{w}(t)$ at $t = t_n + \Delta t$. The details of the analysis can be found in [21]. Thus, based on a time accurate solution $\partial \mathcal{L} / \partial t$, a fourth-order temporal accuracy can be achieved from the two-stage discretization of Eq. (1) through Eq. (3) and Eq. (4). The extension of the above technique to get even higher-order accuracy, such as the fifth-order one, is presented in Appendix.

We apply this approach for conservation laws

$$\frac{\partial \mathbf{w}}{\partial t} + \frac{f(\mathbf{w})}{\partial x} = 0, \quad (5)$$

where \mathbf{w} is a conservative variable and $f(\mathbf{w})$ is the corresponding flux, which includes all terms related to the viscous heat conducting flow. The semi-discrete form of a finite volume scheme for equations Eq. (5) can be written as

$$\frac{\partial \mathbf{w}_i}{\partial t} = \mathcal{L}_i(\mathbf{w}) = -\frac{1}{\Delta x_i} (\mathbf{f}_{i+1/2} - \mathbf{f}_{i-1/2}), \quad (6)$$

where \mathbf{w}_i are the cell averaged conservative variables of the cell $I_i = [x_{i-1/2}, x_{i+1/2}]$, $\mathbf{f}_{i+1/2}$ are the fluxes at the cell interface $x = x_{i+1/2}$, and $\Delta x_i = x_{i+1/2} - x_{i-1/2}$. A similar finite volume formulation can be obtained in two- and three-dimensional cases. Then Eq. (6) falls into the framework of the two-stage L-W time stepping. The theoretical analysis for the time accuracy of the above two-stage method is for the hyperbolic system with $\mathcal{L}(\mathbf{w})$ only. For the NS equations, \mathcal{L} depends on both \mathbf{w} and $\nabla \mathbf{w}$, such as $\mathcal{L}(\mathbf{w}, \nabla \mathbf{w})$. Therefore, the time accuracy of the two-stage method will depend on the viscous and heat conducting terms as well. The detailed formulation will be presented for the GKS specifically.

3. A fourth-order gas-kinetic scheme

The similarity between the generalized Riemann problem (GRP) solver and the gas-kinetic scheme has been studied in [22]. In both schemes, the spatial and temporal accuracy are coupled through a generalized Lax–Wendroff-type procedure for the discontinuous cases, and a single stage time integration is used for the flux transport across a cell interface for the second-order schemes. In this section, a fourth-order gas-kinetic scheme from a second-order flux function will be constructed through a two-stage time discretization framework of Eq. (3) and Eq. (4) for the Euler and Navier–Stokes solutions.

3.1. Second-order gas-kinetic flux solver

The two-dimensional BGK equation can be written as [4],

$$f_t + \mathbf{u} \cdot \nabla f = \frac{g - f}{\tau}, \quad (7)$$

where f is the gas distribution function, g is the corresponding equilibrium state, and τ is the collision time. The collision term satisfies the compatibility condition

$$\int \frac{g - f}{\tau} \psi d\Xi = 0, \quad (8)$$

where $\psi = (1, u, v, \frac{1}{2}(u^2 + v^2 + \xi^2))^T$, $d\Xi = dudvd\xi^1 \dots d\xi^K$, K is the number of internal degrees of freedom, i.e. $K = (4 - 2\gamma)/(\gamma - 1)$ for two-dimensional flows, and γ is the specific heat ratio. The conservative variables are denoted as $W = (\rho, \rho U, \rho V, \rho E)^T$. In the smooth region, the gas distribution function can be expanded as

$$f = g - \tau D_{\mathbf{u}} g + \tau D_{\mathbf{u}} (\tau D_{\mathbf{u}}) g - \tau D_{\mathbf{u}} [\tau D_{\mathbf{u}} (\tau D_{\mathbf{u}}) g] + \dots,$$

where $D_{\mathbf{u}} = \partial/\partial t + \mathbf{u} \cdot \nabla$. By truncating on different orders of τ , the corresponding macroscopic equations can be derived. For the Euler equations, the zeroth order truncation is taken, i.e. $f = g$. For the Navier–Stokes equations, the first order truncation is used,

$$f = g - \tau (u g_x + v g_y + g_t). \quad (9)$$

Based on the higher order truncations, the Burnett and super-Burnett equations can be obtained [6,44,40].

In order to update the flow variables, the flux is based on the integral solution of gas distribution function from the BGK equation at a cell interface,

$$f(x_{i+1/2}, t, u, v, \xi) = \frac{1}{\tau} \int_0^t g(x', y', t', u, v, \xi) e^{-(t-t')/\tau} dt' + e^{-t/\tau} f_0(-ut, y - vt, u, v, \xi), \quad (10)$$

where $x_{i+1/2} = 0$ is the location of the cell interface, $x_{i+1/2} = x' + u(t - t')$ and $y = y' + v(t - t')$ are the trajectory of particles, f_0 is the initial gas distribution function, and g is the corresponding equilibrium state. According to Eq. (10), the time dependent gas distribution function $f(x_{i+1/2}, t, u, v, \xi)$ at the cell interface $x_{i+1/2}$ can be expressed as [42,41],

$$\begin{aligned} f(x_{i+1/2}, t, u, v, \xi) &= (1 - e^{-t/\tau}) g_0 + ((t + \tau) e^{-t/\tau} - \tau) (\bar{a}_1 u + \bar{a}_2 v) g_0 \\ &\quad + (t - \tau + \tau e^{-t/\tau}) \bar{A} g_0 \\ &\quad + e^{-t/\tau} g_r [1 - (\tau + t)(a_{1r} u + a_{2r} v) - \tau A_r] H(u) \\ &\quad + e^{-t/\tau} g_l [1 - (\tau + t)(a_{1l} u + a_{2l} v) - \tau A_l] (1 - H(u)). \end{aligned} \quad (11)$$

Based on the spatial reconstruction of macroscopic flow variables, which will be given in the next subsection, the conservative variables W_l and W_r on the left and right hand sides of a cell interface, and the corresponding equilibrium states g_l and g_r , can be determined. Their spatial derivatives in both normal and tangential directions, such as $(a_{1l}, a_{1r}, a_{2l}, a_{2r})$, are related to the normal and tangential derivatives of the initial macroscopic flow variables. The time derivatives (A_l, A_r) can be obtained from the requirement on the first-order Chapman–Enskog expansion, such as

$$\int g_l (a_{1l} u + a_{2l} v + A_l) \psi d\Xi = 0 \quad , \quad \int g_r (a_{1r} u + a_{2r} v + A_r) \psi d\Xi = 0. \quad (12)$$

Through the compatibility condition Eq. (8), the conservative variables W_0 and the equilibrium state g_0 at the cell interface can be determined as follows,

$$\int \psi g_0 d\Xi = W_0 = \int_{u>0} \psi g_l d\Xi + \int_{u<0} \psi g_r d\Xi. \quad (13)$$

Then, with the spatial derivatives of macroscopic flow variables across and along a cell interface and the compatibility condition, the coefficients related to the spatial derivatives in the equilibrium state in Eq. (11), such as (\bar{a}_1, \bar{a}_2) , and its time derivative \bar{A} , can be fully obtained by,

$$\langle \bar{a}_1 \rangle = \frac{\partial \bar{W}}{\partial x}, \quad \langle \bar{a}_2 \rangle = \frac{\partial \bar{W}}{\partial y}, \quad \langle \bar{a}_1 u + \bar{a}_2 v + \bar{A} \rangle = 0, \quad (14)$$

where $\langle \dots \rangle$ are the moments of the equilibrium gas distribution function g_0 , and defined by

$$\langle \dots \rangle = \int g_0(\dots) \psi d\Xi.$$

More details of the gas-kinetic scheme can be found in [41].

For the Euler solution, in a well-resolved region with continuous flow distributions across a cell interface, i.e. $g_l = g_r$, $a_{1l} = a_{1r} = \bar{a}_1$, $a_{2l} = a_{2r} = \bar{a}_2$, $A_l = A_r = \bar{A}$, and $\tau = 0$, the time dependent gas distribution function in Eq. (11) for the inviscid smooth flow goes to,

$$f(x_{i+1/2}, t, u, v, \xi) = g(1 + \bar{A}t). \tag{15}$$

For the viscous flow with $\tau \neq 0$, in a well-resolved region, the second-order gas-kinetic distribution function (11) goes to

$$f(x_{i+1/2}, t, u, v, \xi) = g(1 - \tau(\bar{a}_1 u + \bar{a}_2 v + \bar{A}) + \bar{A}t). \tag{16}$$

Compared with the inviscid flow, the temporal derivative of the viscous term $-\tau(\bar{a}_1 u + \bar{a}_2 v + \bar{A})g$ in the Navier–Stokes distribution function Eq. (9) is not included. So, an error on the order $\mathcal{O}(\tau \Delta t)$ is kept for the Navier–Stokes equations. In the continuum flow regime, $\tau \ll \Delta t$ is usually satisfied and the second-order accuracy can be achieved for the single-stage second order gas-kinetic scheme [41].

For the current fourth order scheme, we need to further improve the time accuracy for the viscous solution. Based on the above second order solution (11), the accuracy for the viscous term can be hardly improved further. Here, we can include the time derivative of the viscous term in the flux function. In a smooth region, Eq. (16) should be extended to

$$f = g[1 - \tau(\bar{a}_1 u + \bar{a}_2 v + \bar{A})] + g[\bar{A} - \tau(\bar{A}\bar{a}_1 + \bar{b}_1)u + (\bar{A}\bar{a}_2 + \bar{b}_2)v + (\bar{A}^2 + \bar{B})]t, \tag{17}$$

where the coefficients for the additional terms are defined by

$$\bar{B} = (\partial \bar{A} / \partial t), \bar{b}_1 = (\partial \bar{a}_1 / \partial t) = (\partial \bar{A} / \partial x), \bar{b}_2 = (\partial \bar{a}_2 / \partial t) = (\partial \bar{A} / \partial y).$$

All these additional terms can be constructed from a higher-order expansion of the equilibrium state around a cell interface, where both first and second-order spatial derivatives of macroscopic variables are needed. Fortunately, all these terms have been used in the third-order GKS [24,28], which can be borrowed here directly. In the smooth region, based on Eq. (17) the two-stage GKS will have a temporal order of accuracy $\mathcal{O}(\tau^2 \Delta t)$, and the additional terms in Eq. (17) different from Eq. (16) can be added to Eq. (11). Numerically, Eq. (17) will be used for the accuracy test for the Navier–Stokes solutions only. In other computations, Eq. (11) will still be used for both the Euler and NS solutions. In practical computations, the time between particle collisions τ is usually much smaller than the time step Δt .

The coupling between the spatial and temporal derivatives in the time evolution of the gas kinetic distribution function of GKS is based on the Euler equations, such as Eq. (12), and this process can be continued with additional spatial or temporal derivatives to Eq. (12), such as the construction of additional terms \bar{b}_1 , \bar{b}_2 , and \bar{B} in Eq. (17). For a higher temporal accuracy of the NS solutions, if the coupling between the spatial and temporal derivatives is constructed through the NS equations, this process could make the scheme extremely complicated, and introduce uncertainties in the underlying physics since the Cauchy–Kovalevskaya approach itself is for the hyperbolic equations only. Theoretically, it is still a challenging problem physically and numerically for the development of higher order temporal accurate scheme for the NS equations.

3.2. Spatial reconstruction

The above time evolution solution is based on the high-order initial reconstruction for macroscopic flow variables. Without special statement, the fifth-order WENO-JS reconstruction is adopted in this study [15].

For one dimensional computation, W_l , W_r and W_0 corresponding to the equilibrium states g_l , g_r and g_0 in Eq. (11) can be constructed at the cell interface $x_{i+1/2}$. The spatial derivatives $\partial W / \partial x$ are also given based on the reconstruction. Especially, for the determination of the equilibrium state g_0 across the cell interface with a fifth-order of accuracy, the conservative variables around the cell interface can be expanded as

$$\bar{W}(x) = W_0 + S_1(x - x_*) + \frac{1}{2}S_2(x - x_*)^2 + \frac{1}{6}S_3(x - x_*)^3 + \frac{1}{24}S_4(x - x_*)^4.$$

With the following conditions,

$$\int_{I_{i+k}} \bar{W}(x) = W_{i+k}, k = -1, \dots, 2,$$

the derivatives are given by

$$\begin{aligned} \overline{W}_x &= S_1 = \left[-\frac{1}{12}(W_{i+2} - W_{i-1}) + \frac{5}{4}(W_{i+1} - W_i) \right] / \Delta x, \\ \overline{W}_{xx} &= S_2 = \left[-\frac{1}{8}(W_{i+2} + W_{i-1}) + \frac{31}{8}(W_{i+1} + W_i) - \frac{15}{2}W_0 \right] / \Delta x^2. \end{aligned}$$

For two dimensional computation, the fifth-order Gauss quadrature is used to achieve the accuracy in space

$$\frac{1}{\Delta y} \int_{y_{j-1/2}}^{y_{j+1/2}} F(W(x_{i+1/2}, y, t)) dy = \sum_{\ell=1}^k \omega_\ell F(W(x_{i+1/2}, y_\ell, t)), \tag{18}$$

where $y_\ell \in [y_{j-1/2}, y_{j+1/2}]$, $\ell = 1, \dots, 3$ are the Gauss quadrature points, and ω_ℓ are corresponding weights. Based on the tangential reconstruction, the tangential derivatives at each Gauss quadrature points can be obtained.

3.3. Two-stage gas-kinetic scheme

In this section, a two-stage fourth-order gas-kinetic scheme will be presented based on the time-dependent gas distribution function (11) at each cell interface.

For the gas-kinetic scheme, the gas evolution is a relaxation process from kinetic to hydrodynamic scale through the exponential function, and the corresponding flux is a complicated function of time. In order to obtain the time derivatives of the flux function at t_n and $t_* = t_n + \Delta t/2$, the flux function should be approximated as a linear function of time within a time interval. Let's first introduce the following notation,

$$\mathbb{F}_{i+1/2}(W^n, \delta) = \int_{t_n}^{t_n+\delta} F_{i+1/2}(W^n, t) dt = \int_{t_n}^{t_n+\delta} \int u \psi f(x_{i+1/2}, t, u, v, \xi) d\Xi dt.$$

In the time interval $[t_n, t_n + \Delta t]$, the flux is expanded as the following linear form

$$F_{i+1/2}(W^n, t) = F_{i+1/2}^n + \partial_t F_{i+1/2}^n (t - t_n). \tag{19}$$

The coefficients $F_{i+1/2}^n$ and $\partial_t F_{i+1/2}^n$ can be determined as follows,

$$F_{i+1/2}(W^n, t_n) \Delta t + \frac{1}{2} \partial_t F_{i+1/2}(W^n, t_n) \Delta t^2 = \mathbb{F}_{i+1/2}(W^n, \Delta t), \tag{20}$$

$$\frac{1}{2} F_{i+1/2}(W^n, t_n) \Delta t + \frac{1}{8} \partial_t F_{i+1/2}(W^n, t_n) \Delta t^2 = \mathbb{F}_{i+1/2}(W^n, \Delta t/2). \tag{21}$$

By solving the linear system, we have

$$\begin{aligned} F_{i+1/2}(W^n, t_n) &= (4\mathbb{F}_{i+1/2}(W^n, \Delta t/2) - \mathbb{F}_{i+1/2}(W^n, \Delta t)) / \Delta t, \\ \partial_t F_{i+1/2}(W^n, t_n) &= 4(\mathbb{F}_{i+1/2}(W^n, \Delta t) - 2\mathbb{F}_{i+1/2}(W^n, \Delta t/2)) / \Delta t^2. \end{aligned} \tag{22}$$

Similarly, $F_{i+1/2}(W^*, t_*)$, $\partial_t F_{i+1/2}(W^*, t_*)$ for the intermediate state can be constructed. For the two-dimensional computation, the corresponding fluxes in the y -direction can be obtained as well.

Eq. (11) is the general form of the numerical flux with a discontinuous initial data. In the discontinuous region, the time evolution of the flux function is a complicated function of time. We have to use Eq. (22) to extract the averaged flux and its first-order time derivative in a reasonable time scale. Certainly, this evaluation may introduce something which is different from the exact time-dependent kinetic evolution mechanism, such as the free transport from a discontinuity. However, the order of the scheme cannot be theoretically defined in a discontinuous region. Fortunately, in smooth region the gas distribution functions Eq. (11) will reduce to Eq. (16), and Eq. (22) gives an exact solution, which is independent of the time scale used for evaluating the averaged flux and its time derivative.

With these notations, the two-stage algorithm for both the Euler and Navier–Stokes equations is given as follows

- (i) With the initial reconstruction, update W_{ij}^* at $t_* = t_n + \Delta t/2$ by

$$\begin{aligned} W_{ij}^* &= W_{ij}^n - \frac{1}{\Delta x} [\mathbb{F}_{i+1/2,j}(W^n, \Delta t/2) - \mathbb{F}_{i-1/2,j}(W^n, \Delta t/2)] \\ &\quad - \frac{1}{\Delta y} [\mathbb{G}_{i,j+1/2}(W^n, \Delta t/2) - \mathbb{G}_{i,j-1/2}(W^n, \Delta t/2)], \end{aligned}$$

and compute the fluxes and their derivatives by Eq. (22) for future use,

$$F_{i+1/2,j}(W^n, t_n), G_{i,j+1/2}(W^n, t_n), \partial_t F_{i+1/2,j}(W^n, t_n), \partial_t G_{i,j+1/2}(W^n, t_n).$$

Table 1

The computational cost for different schemes on the structured mesh with the same WNEO reconstruction with conservative and characteristic variables.

Schemes	Type of flux	Stage	Number of flux at each interface	Time (conser.)	Time (charac.)
2nd-order GKS	2nd-order flux	1	1	0.70489 s	0.84287 s
3rd-order GKS	3rd-order flux	1	1	1.24681 s	1.38178 s
4th-order GKS	2nd-order flux	2	3	1.95370 s	2.20566 s

(ii) Reconstruct intermediate value W_{ij}^* , and compute

$$\partial_t F_{i+1/2,j}(W^*, t_*), \quad \partial_t G_{i,j+1/2}(W^*, t_*),$$

where the derivatives are determined by Eq. (22) in the time interval $[t_*, t_* + \Delta t]$.

(iii) Update W_{ij}^{n+1} by

$$W_{ij}^{n+1} = W_{ij}^n - \frac{\Delta t}{\Delta x} [\mathcal{F}_{i+1/2,j}^n - \mathcal{F}_{i-1/2,j}^n] - \frac{\Delta t}{\Delta y} [\mathcal{G}_{i,j+1/2}^n - \mathcal{G}_{i,j-1/2}^n],$$

where $\mathcal{F}_{i+1/2,j}^n$ and $\mathcal{G}_{i,j+1/2}^n$ are the numerical fluxes and expressed as

$$\mathcal{F}_{i+1/2,j}^n = F_{i+1/2,j}(W^n, t_n) + \frac{\Delta t}{6} [\partial_t F_{i+1/2,j}(W^n, t_n) + 2\partial_t F_{i+1/2,j}(W^*, t_*)],$$

$$\mathcal{G}_{i,j+1/2}^n = G_{i,j+1/2}(W^n, t_n) + \frac{\Delta t}{6} [\partial_t G_{i,j+1/2}(W^n, t_n) + 2\partial_t G_{i,j+1/2}(W^*, t_*)].$$

For the flux transport across a cell interface, the Gaussian quadratures Eq. (18) are used.

In summary, based on the distribution function (17) for the flux in the smooth region, the above scheme solves the Euler equations with the leading error of $\mathcal{O}((\Delta x)^5, (\Delta t)^4)$, and the NS equations with the error of $\mathcal{O}(\Delta x)^5, \tau^2 \Delta t$. For most calculations in the next section, the flux function from the distribution function (11) is usually used. With such a distribution function, in smooth region the above scheme solves the Euler equations with the leading error $\mathcal{O}((\Delta x)^5, (\Delta t)^4)$, and the NS equations with the error $\mathcal{O}(\Delta x)^5, \tau \Delta t$. Fortunately, for many flow computations the condition $\tau \ll \Delta t$ is usually satisfied.

4. Numerical tests

In this section, numerical tests for both inviscid and viscous flow will be presented to validate the current scheme. For the inviscid flow, the collision time τ takes

$$\tau = \epsilon \Delta t + C \left| \frac{p_l - p_r}{p_l + p_r} \right| \Delta t,$$

where $\epsilon = 0.01$ and $C = 1$. For the viscous flow, the collision time is defined by

$$\tau = \frac{\nu}{p} + C \left| \frac{p_l - p_r}{p_l + p_r} \right| \Delta t,$$

where p_l and p_r denote the pressure on the left and right sides of the cell interface, ν is the dynamic viscous coefficient, and p is the pressure at the cell interface. In smooth flow region, it will reduce to $\tau = \nu/p$. The ratio of specific heats takes $\gamma = 1.4$. The reason for including artificial dissipation through the additional term in the particle collision time is to enlarge the kinetic scale physics in the discontinuous region for the construction of a numerical shock structure, and to keep the non-equilibrium property in the shock region through the particle free transport mechanism.

For the smooth flow, the WENO reconstruction can be used directly on the conservative flow variables. For the flow with strong discontinuity, the characteristic variables can be used in the reconstruction. Based on $A_{i+1/2,j} = (\partial F / \partial W)_{W=W^*}$, where W are the conservative variables, $F(W)$ are the corresponding fluxes, and $W^* = (W_{i,j} + W_{i+1,j})/2$, the cell averaged and pointwise conservative variables can be projected into the characteristic field by $\omega = R^{-1}W$, where R is the matrix corresponding to right eigenvectors of A . The reconstruction scheme is applied on the characteristic variables ω . With the reconstructed polynomials for characteristic variables, the conservative flow variables can be recovered by the inverse projection.

In terms of computational cost, the two-dimensional Riemann problems are tested. As a reference, the CPU times for different schemes are obtained with 100×100 cells and 10 time steps with Intel Core i7-4770 CPU @ 3.40 GHz. Based on the same WENO reconstruction, the CPU times for the second-order GKS [42,45], the single stage third-order GKS [24,28], and the current two-stage fourth-order GKS are given in Table 1, where both conservative and characteristic reconstructions are used.

For the fourth-order GKS, the computational cost is about 3 times of that of second-order scheme. Since the fourth-order GKS calculates 6 fluxes at each cell interface in comparison with 1 flux for the second-order scheme, the computational time difference means that the reconstruction takes the main part in the total computational cost, because the fourth-order scheme only takes two reconstructions instead of one in the second-order scheme. However, in order to get the same accuracy as that of the fourth-order scheme, the second-order method needs refine the mesh, at least once. In the two-dimensional calculation, the computational cost for one mesh refinement will be increased by 8 times. Therefore, the fourth-order scheme is more efficient than the second order method.

Here we evaluate the computational costs of the WENO-type reconstruction and the flux evaluation quantitatively. The time for each reconstruction is denoted by T_R , the time for second-order gas-kinetic solver is T_{2nd} , and the time for third-order flux solver is T_{3rd} . According to the data provided in the Table 1, we can estimate the time used for the computations of flux and reconstruction with the following relations,

$$T_R + 2T_{2nd} = 0.84287 \text{ s},$$

$$T_R + 2T_{3rd} = 1.38178 \text{ s},$$

$$2T_R + 12T_{2nd} = 2.20566 \text{ s},$$

where the estimation is based on the characteristic variable reconstruction and each flux is shared by two cells. Thus, the time for reconstruction is $T_R = 0.71289 \text{ s}$, the time for second-order gas-kinetic flux solver is $T_{2nd} = 0.06499 \text{ s}$ and the time for third-order gas-kinetic flux solver is $T_{3rd} = 0.33445 \text{ s}$. For classical fourth-order Runge–Kutta schemes, the computational cost for the four spatial reconstructions alone will become much higher than the cost of the fourth-order gas-kinetic scheme with two reconstructions and full flux function evaluations,

$$4T_R = 2.85156 \text{ s} > 2T_R + 12T_{2nd} = 2.20566 \text{ s}.$$

Similar estimation can be done for the conservative variables reconstruction. Even without counting on the cost of the flux evaluation in the traditional fourth-order Runge–Kutta method, such as those commonly used with the Lax–Friedrichs flux, the current fourth-order GKS is still more efficient than the classical method for the Euler solutions.

Since higher-order scheme does have advantages in comparison with lower order method, it is worth to construct the two-stage fifth-order GKS from the third-order GKS flux function, see Appendix. Besides the computational cost, another important property of the fourth-order GKS is its accuracy and robustness. As tested next, it clearly indicates that the fourth-order scheme is very accurate and is as robust as the second-order one. The accuracy of the scheme is closely related to the time-dependent gas evolution model, the multi-dimensionality for the explicit inclusion of both normal and tangential derivatives of flow variables around a cell interface, and the unified treatment of the inviscid and viscous terms.

4.1. Accuracy tests

The first case is the advection of density perturbation, and the initial condition is set as follows

$$\rho(x) = 1 + 0.2 \sin(\pi x), \quad U(x) = 1, \quad p(x) = 1, \quad x \in [0, 2].$$

The periodic boundary condition is adopted, and the analytic solution is

$$\rho(x, t) = 1 + 0.2 \sin(\pi(x - t)), \quad U(x, t) = 1, \quad p(x, t) = 1.$$

In the computation, a uniform mesh with N points is used.

In this test, a fixed CFL number $CFL = 0.4$ is used for different meshes. As analyzed in the previous section, with the fifth-order spatial reconstruction, the leading truncation error in the inviscid case from the fourth-order GKS is $\mathcal{O}(\Delta x^5 + \Delta t^4)$. With the fixed CFL number, we have $\Delta t = c\Delta x$ and the leading term becomes $\mathcal{O}(\Delta x^5 + \Delta t^4) \sim \mathcal{O}(\Delta x^5 + c^4\Delta x^4)$. With the mesh refinement, the order of accuracy will converge to 4. The L^1 and L^2 errors and orders at $t = 2$ are presented in Table 2. The expected order accuracy can be achieved. As a comparison, with the original second-order GKS, the leading error is on the order of $\mathcal{O}(\Delta x^5 + \Delta t^2) \sim \mathcal{O}(\Delta x^5 + c^2\Delta x^2)$. With the identical spatial reconstruction and CFL number $CFL = 0.4$, the L^1 and L^2 errors and orders at $t = 2$ are presented in Table 3. With the mesh refinement, the temporal error becomes dominant and the order reduces to 2 for the second-order scheme. For the same accuracy, the second-order scheme requires a mesh size which is 1/8 of the mesh size of the fourth-order scheme. With the consideration of the time step, the fourth-order scheme is at least 16 times more efficient than the second-order one.

The next test is the isotropic vortex propagation problem. The mean flow is $(\rho, U, V, p) = (1, 1, 1, 1)$, and an isotropic vortex is added to the mean flow, i.e., with perturbation in u, v and temperature $T = p/\rho$, and no perturbation in entropy $S = p/\rho^\gamma$. The perturbation is given by

$$(\delta U, \delta V) = \frac{\epsilon}{2\pi} e^{\frac{(1-r^2)}{2}} (-y, x), \quad \delta T = -\frac{(\gamma - 1)\epsilon^2}{8\gamma\pi^2} e^{1-r^2}, \quad \delta S = 0,$$

where $r^2 = x^2 + y^2$ and the vortex strength $\epsilon = 5$. The computational domain is $[-5, 5] \times [-5, 5]$, the periodic boundary conditions are imposed on the boundaries in both x and y directions. The exact solution is the perturbation which propa-

Table 2

Accuracy test for the advection of density perturbation by the fourth-order GKS.

Mesh	L^1 error	Convergence order	L^2 error	Convergence order
20	4.4759E-004		3.7653E-004	
40	1.3764E-005	5.0231	1.1504E-005	5.0324
80	4.2791E-007	5.0075	3.4744E-007	5.0493
160	1.3354E-008	5.0018	1.0644E-008	5.0286
320	4.1722E-010	5.0003	3.2940E-010	5.0140
640	1.3039E-011	4.9998	1.0250E-011	5.0060
1280	4.5156E-013	4.8517	3.5536E-013	4.8502

Table 3

Accuracy test for the advection of density perturbation by the second-order GKS.

Mesh	L^1 error	Convergence order	L^2 error	Convergence order
20	4.5359E-004		4.0178E-004	
40	6.5305E-005	2.7961	5.1786E-005	2.9557
80	1.6435E-005	1.9904	1.2899E-005	2.0053
160	4.1119E-006	1.9988	3.2291E-006	1.9980
320	1.0280E-006	1.9998	8.0743E-007	1.9997
640	2.5702E-007	1.9999	2.0186E-007	1.9999
1280	6.4255E-008	1.9999	5.0465E-008	1.9999

Table 4Accuracy of the fourth-order GKS for the isentropic vortex propagation at time $t = 10$.

Mesh	L^1 error	convergence order	L^∞ error	Convergence order
20×20	1.98E-3		3.79E-2	
40×40	1.69E-4	3.55	8.08E-3	2.23
80×80	8.92E-6	4.24	4.10E-4	4.30
160×160	2.31E-7	5.27	5.29E-6	6.28
320×320	7.40E-9	4.96	2.09E-7	4.66
640×640	2.76E-10	4.74	7.09E-9	4.88

Table 5 L_1 norm of $\|U_N - U_{N/2}\|$ for the Euler equations and the Navier–Stokes solutions with $\nu = 0.0001$ and 0.00001 .

N	Euler	N-S $\nu = 10^{-5}$	N-S $\nu = 10^{-4}$
16	1.00324E-002	1.01422E-002	1.01252E-002
32	6.28901E-004	6.35975E-004	6.36744E-004
64	2.02624E-005	2.05168E-005	2.03871E-005
128	6.27890E-007	6.30078E-007	7.86406E-007
256	2.00390E-008	3.45703E-008	2.80859E-007

gates with the velocity $(1, 1)$. The L^1 and L^∞ errors and orders at $t = 10$ with $N \times N$ uniform mesh cells are presented in Table 4, where the expected accuracy can be achieved for the two dimensional inviscid computation.

The last accuracy test is for the Navier–Stokes solutions. Because there is no specific test case available with analytical solution for the compressible time-dependent Navier–Stokes equations, the advection of a density perturbation with the effect of both viscosity and heat conductivity is adopted. The identical initial condition as the first accuracy test case, and periodic boundary condition are used. The viscous coefficients $\nu = 0.0001$ and 0.00001 are chosen with the collision term $\tau = \nu/p$, which is independent of mesh size. A fixed CFL number $CFL = 0.2$ and a uniform mesh with N cells are used. The solutions with N mesh cells are denoted as U_N . The L_1 norm for $\|U_N - U_{N/2}\|_1$ is given in Table 5 and Fig. 1. The density distributions for $\nu = 0.0001$ with 16 and 256 mesh cells are also presented in Fig. 1. For the Euler solutions, the theoretical accuracy can be always kept. For the Navier–Stokes solutions with $\nu = 0.00001$, the particle collision time τ is less than the time step even for the much refined mesh, the expected order of accuracy is obtained. However, for the case with $\nu = 0.0001$, the particle collision time becomes relative large. As the time step Δt reduces with the mesh refinement, the order of accuracy deteriorates. In the computation, as shown in the right sub-figure of Fig. 1, an accurate NS solution can be obtained with a relatively coarse mesh without using such a refinement. So, the reduction of the order of accuracy in the refined mesh case will not hurt too much to the quality of the NS solutions.

4.2. One dimensional Riemann problems

For one-dimensional case, two Riemann problems are considered. The first one is the Sod problem. The computational domain is $[0, 1]$ with 100 uniform mesh points and with non-reflecting boundary condition on both ends. The initial condition is given by

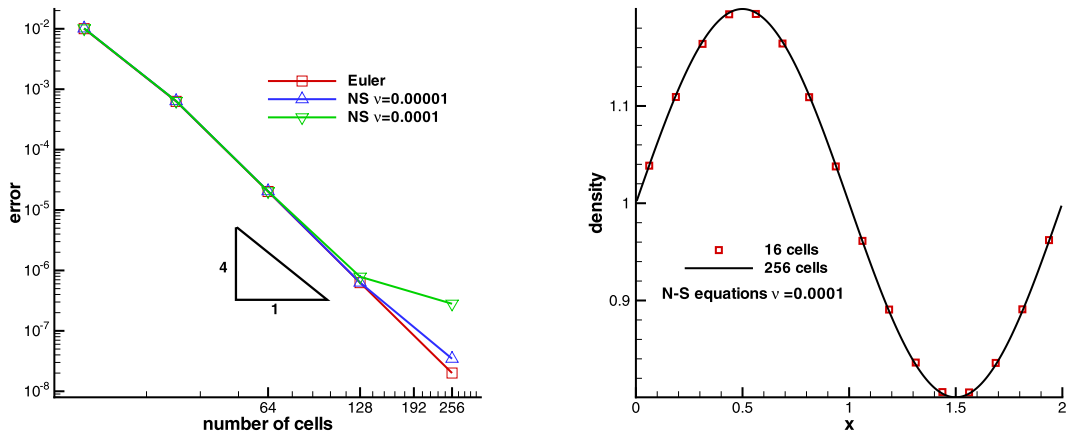


Fig. 1. Order of accuracy. L_1 norm of $\|U_N - U_{N/2}\|$ for the Euler and the Navier–Stokes solutions (left), and density distribution for $\nu = 0.0001$ with 16 and 256 mesh points (right).

$$(\rho, U, p) = \begin{cases} (1, 0, 1), & 0 < x < 0.5, \\ (0.125, 0, 0.1), & 0.5 < x < 1. \end{cases}$$

The second one is the Woodward–Colella blast wave problem [39]. The computational domain is $[0, 100]$ with 200 and 400 uniform mesh points. The reflecting boundary conditions are imposed on both ends. The initial conditions are given as follows,

$$(\rho, U, p) = \begin{cases} (1, 0, 1000), & 0 \leq x < 10, \\ (1, 0, 0.01), & 10 \leq x < 90, \\ (1, 0, 100), & 90 \leq x \leq 100. \end{cases}$$

The density, velocity, and pressure distributions for the fourth-order GKS and the exact solutions are presented in Fig. 2 for the Sod problem at $t = 0.2$ and for the blast wave problem at $t = 3.8$. The numerical results agree well with the exact solutions. The scheme can resolve the wave profiles well, particularly for the local extreme values.

In the one-dimensional case, another standard test case is the Shu–Osher shock acoustic interaction [35]. The computational domain is $[-5, 5]$ and the flow field is initialized as

$$(\rho, U, p) = \begin{cases} (3.857134, 2.629369, 10.333333), & x \leq -4, \\ (1 + 0.2 \sin(5x), 0, 1), & -4 < x. \end{cases}$$

Both WENO-JS and WENO-Z [5] reconstructions are used in this case. The computed density profile and local enlargement with 400 grid points at $t = 1.8$ are shown in Fig. 3. WENO-Z reconstruction provides a little bit more accurate solution than that from WENO-JS.

The stability for the current scheme is tested by the Sod problem. The velocity profiles with different CFL numbers from 0.2 to 0.7, are shown in Fig. 4. The scheme is basically stable under the conventional CFL condition. The waves profiles can be well resolved at a CFL number around 0.5. In the following numerical tests, without spacial statement, the CFL number takes a fixed value of 0.4.

4.3. Two-dimensional Riemann problems

In the following, two examples of two-dimensional Riemann problems are considered, which involve the interactions of shocks, the interaction of shocks with vortex sheets, and the interaction of vortices [19,23,12]. The computational domain is $[0, 1] \times [0, 1]$, and the non-reflecting boundary conditions are used in all boundaries. The initial conditions for the first problem are

$$(\rho, U, V, p) = \begin{cases} (1.5, 0, 0, 1.5), & x > 0.5, y > 0.5, \\ (0.5323, 1.206, 0, 0.3), & x < 0.5, y > 0.5, \\ (0.138, 1.206, 1.206, 0.029), & x < 0.5, y < 0.5, \\ (0.5323, 0, 1.206, 0.3), & x > 0.5, y < 0.5. \end{cases}$$

Four initial shock waves interact with each other and result in a more complicated pattern. The density distribution and the local enlargement are given at $t = 0.4$ in Fig. 5 with 400×400 and 800×800 mesh points. From the analysis in [19], the

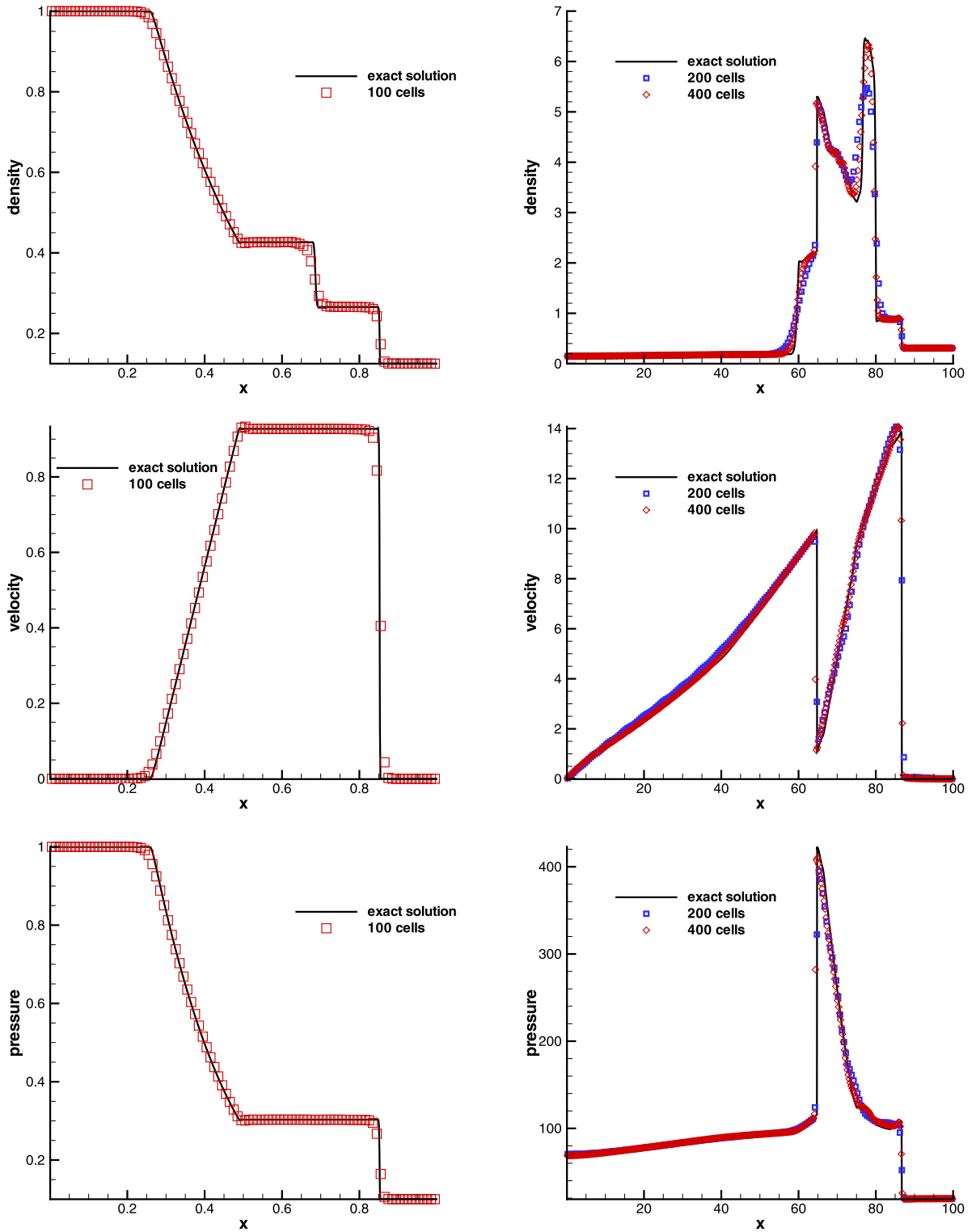


Fig. 2. Sod problem (left): the density, velocity and pressure distributions at $t = 0.2$ with 100 cells, and blast wave problem (right): the density, velocity and pressure distributions at $t = 3.8$ with 200 and 400 cells.

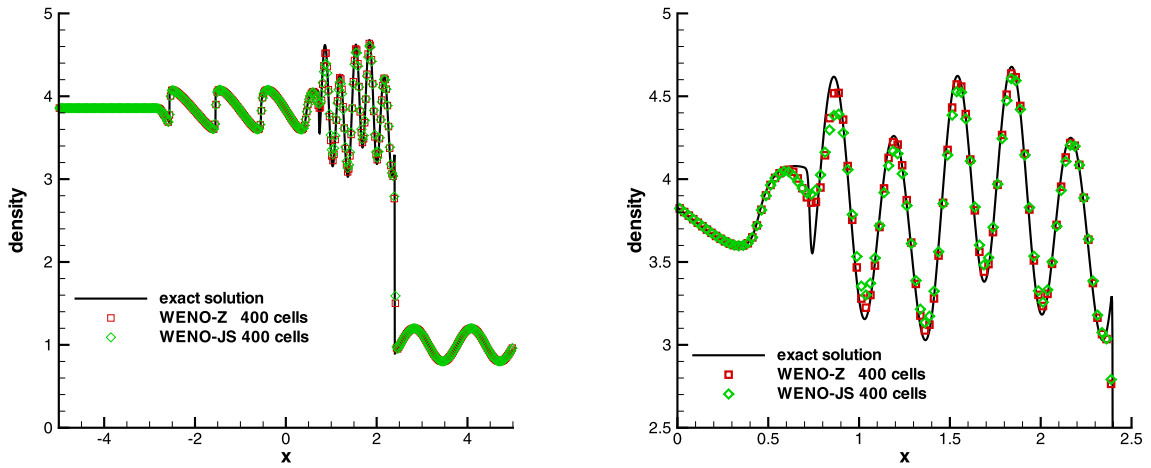


Fig. 3. Shu–Osher shock acoustic-wave interaction. Density distributions for WENO-JS and WENO-Z reconstruction at $t = 1.8$ with 400 cells.

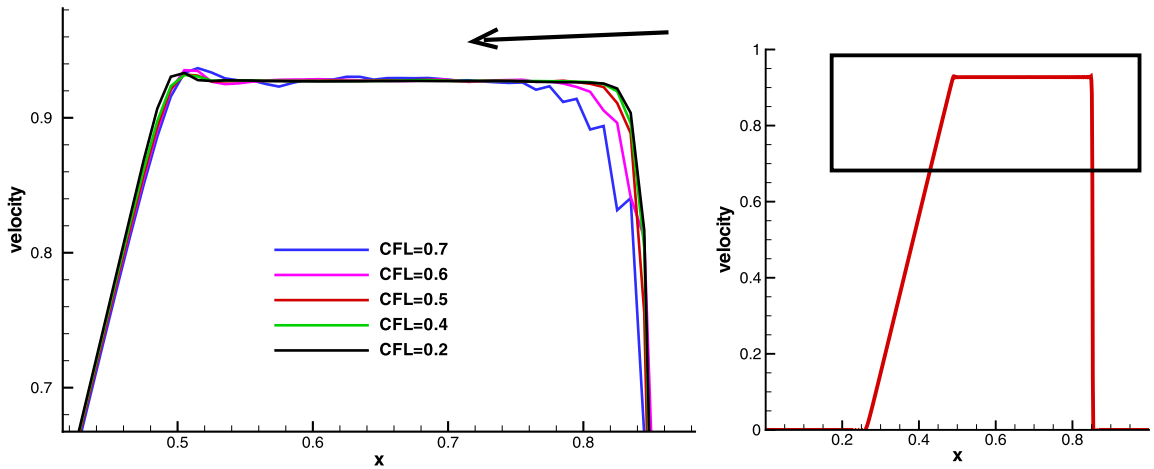


Fig. 4. The stability test for the Sod problem.

initial shock wave S_{23}^- bifurcates at the trip point into a reflected shock wave, a Mach stem, and a slip line. The reflected shock wave interacts with the shock wave S_{12}^- to produce a new shock. The small scale flow structures are well captured by the current scheme.

The initial conditions for the second case are

$$(\rho, U, V, p) = \begin{cases} (1, 0.1, 0.1, 1), & x > 0.5, y > 0.5, \\ (0.5197, -0.6259, 0.1, 0.4), & x < 0.5, y > 0.5, \\ (0.8, 0.1, 0.1, 0.4), & x < 0.5, y < 0.5, \\ (0.5197, 0.1, -0.6259, 0.4), & x > 0.5, y < 0.5. \end{cases}$$

This case is to simulate the interaction of the rarefaction waves and the vortex-sheets. The density distribution at $t = 0.4$ and the local enlargement are given in Fig. 6 with 600×600 and 1000×1000 mesh points. The roll-up is well captured by the current scheme.

4.4. Shock vortex interaction

The interaction between a stationary shock and a vortex for the inviscid flow [15] is presented. The computational domain is taken to be $[0, 2] \times [0, 1]$. A stationary Mach 1.1 shock is positioned at $x = 0.5$ and normal to the x -axis. The left upstream state is $(\rho, U, V, p) = (Ma^2, \sqrt{\gamma}, 0, 1)$, where Ma is the Mach number. A small vortex is obtained through a perturbation on the mean flow with the velocity (U, V) , temperature $T = p/\rho$, and entropy $S = \ln(p/\rho^\gamma)$. The perturbation is expressed as

$$(\delta U, \delta V) = \kappa \eta e^{\mu(1-\eta^2)} (\sin \theta, -\cos \theta),$$

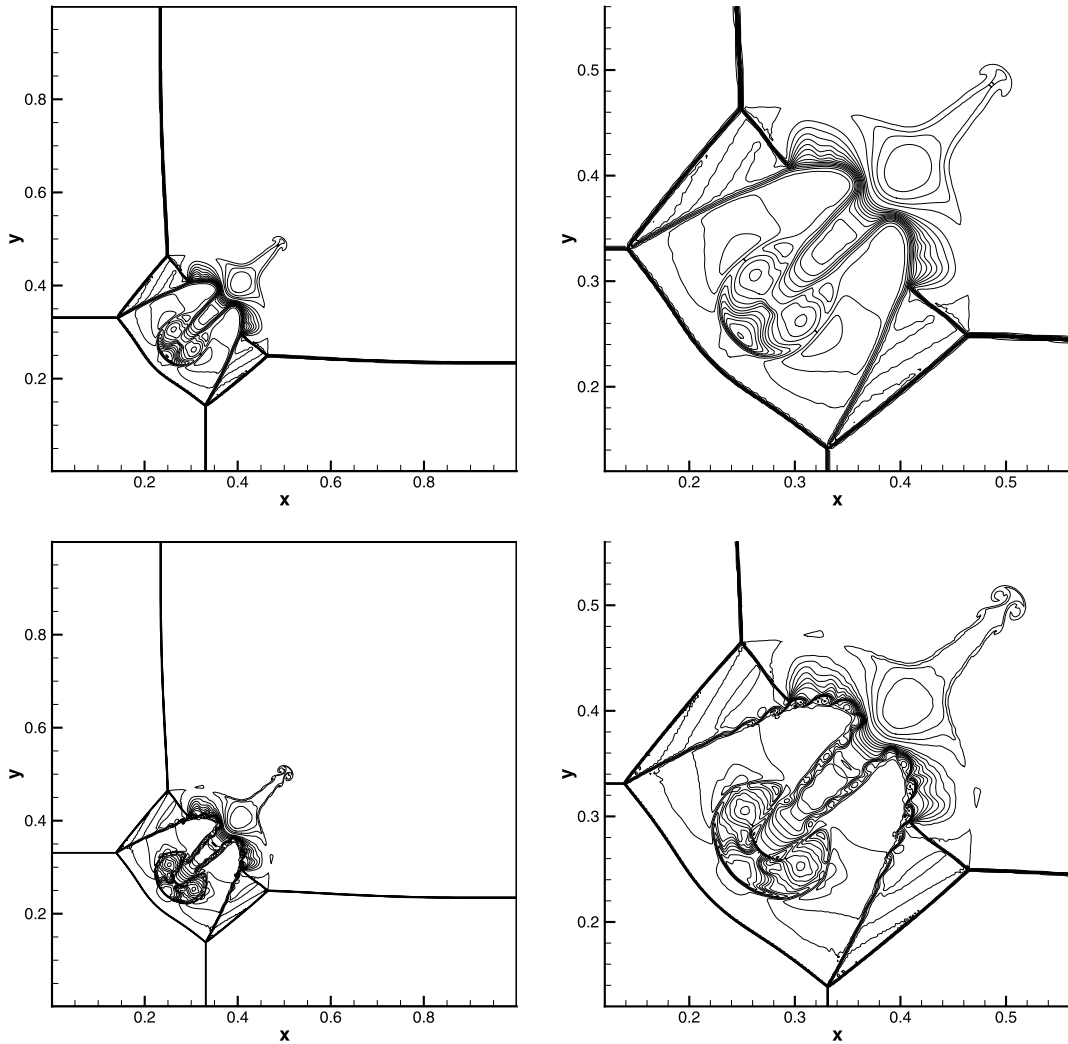


Fig. 5. The density distribution for the first two-dimensional Riemann problem at $t = 0.3$ with 400×400 (top) and 800×800 (bottom) mesh points.

$$\delta T = -\frac{(\gamma - 1)\kappa^2}{4\mu\gamma} e^{2\mu(1-\eta^2)}, \delta S = 0,$$

where $\eta = r/r_c$, $r = \sqrt{(x - x_c)^2 + (y - y_c)^2}$, and $(x_c, y_c) = (0.25, 0.5)$ is the center of the vortex. Here κ indicates the strength of the vortex, μ controls the decay rate of the vortex, and r_c is the critical radius for which the vortex has the maximum strength. In the computation, $\kappa = 0.3$, $\mu = 0.204$, and $r_c = 0.05$. The reflecting boundary conditions are used on the top and bottom boundaries. The pressure distributions with mesh size $\Delta x = \Delta y = 1/200$ at $t = 0, 0.3, 0.6$ and 0.8 are shown in Fig. 7. By $t = 0.8$, one branch of the shock bifurcations has reached the top boundary and been reflected. The reflection is well captured. The detailed density distributions along the center horizontal line with mesh size $\Delta x = \Delta y = 1/50, 1/100$ and $1/200$ at $t = 0.8$ are shown in Fig. 8. The accuracy of the scheme is well demonstrated.

4.5. Double Mach reflection problem

This problem was extensively studied by Woodward and Colella [39] for the inviscid flow. The computational domain is $[0, 4] \times [0, 1]$, and a solid wall lies at the bottom of the computational domain starting from $x = 1/6$. Initially a right-moving Mach 10 shock is positioned at $(x, y) = (1/6, 0)$, and makes a 60° angle with the x -axis. The initial pre-shock and post-shock conditions are

$$(\rho, U, V, p) = (8, 4.125\sqrt{3}, -4.125, 116.5),$$

$$(\rho, U, V, p) = (1.4, 0, 0, 1).$$

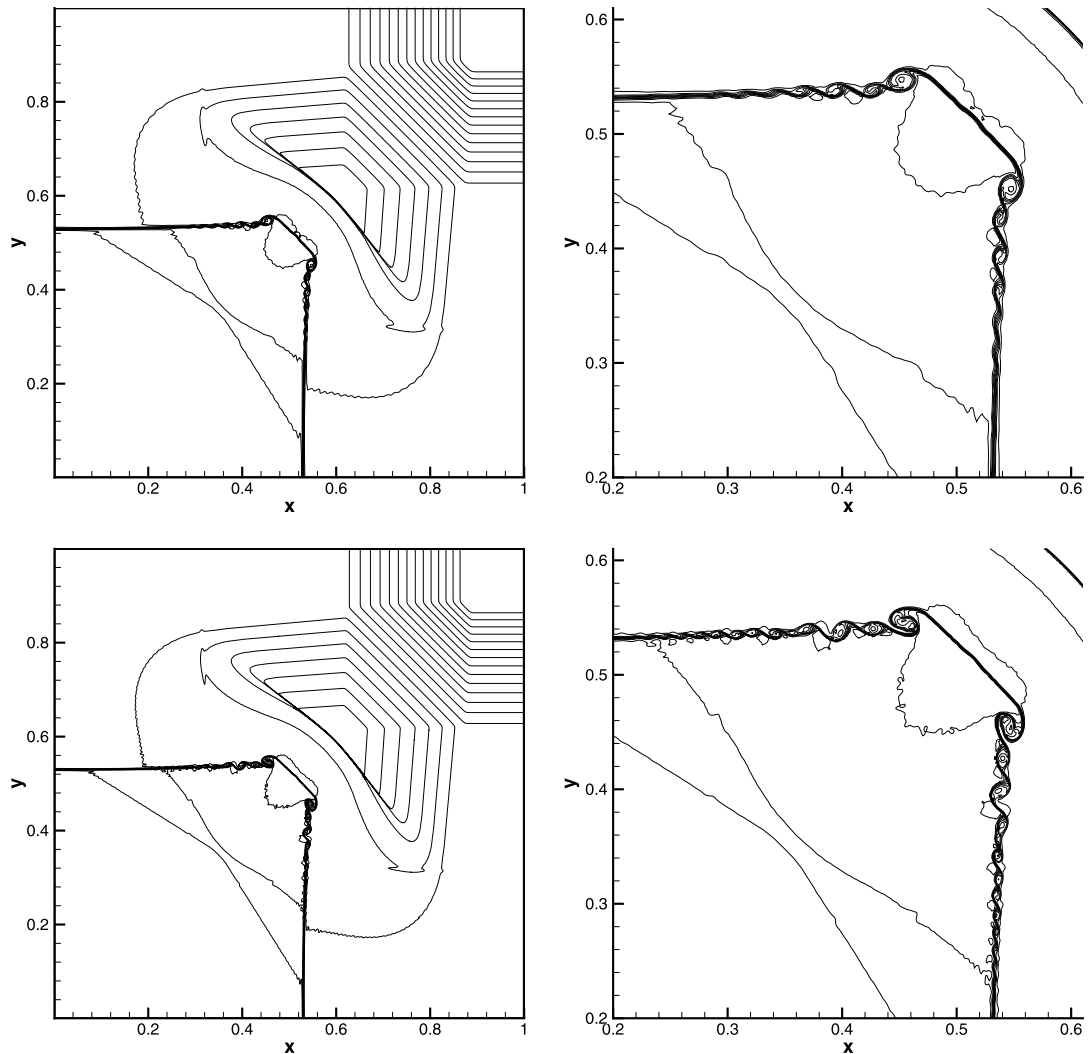


Fig. 6. The density distribution for the second two-dimensional Riemann problem at $t = 0.25$ with 600×600 (top) and 1000×1000 (bottom) mesh points.

The reflecting boundary condition is used at the wall, while for the rest of bottom boundary, the exact post-shock condition is imposed. At the top boundary, the flow variables are set to describe the exact motion of the Mach 10 shock. Both WENO-JS and WENO-Z reconstructions are used in this case. The density distributions with 1440×480 uniform mesh points at $t = 0.2$ for WENO-JS and WENO-Z reconstructions are shown in Fig. 9 and Fig. 10, respectively. The current scheme resolves the flow structure under the triple Mach stem clearly. Compared with the WENO-JS scheme, the WENO-Z reconstruction is less dissipative and the instability of contact line is better resolved.

4.6. Hypersonic flow past a cylinder

In this case, the hypersonic flows impinging on a unit cylinder are tested to validate robustness of the current scheme. The first one is for the inviscid flow, which has been used to compare the solutions from the second-order GRP and GKS [22]. This problem is initialized by a flow moving towards to a cylinder with different Mach numbers. The reflective boundary condition is imposed on the surface of cylinder, and the outflow boundary condition is set on the right boundary. In the computation, 60×100 mesh points are used, which is shown in Fig. 11. The Mach number distributions for the flows with $Ma = 5, 10,$ and 20 are also presented in Fig. 11 as well, which show that the current scheme can capture strong shocks very well without carbuncle phenomenon [31]. The robustness of the scheme is well validated.

The viscous and heat conducting case at high Mach number is also tested. The flow condition is given as $Ma_\infty = 8.03$, $T_\infty = 124.94$ K for the far field, the wall temperature is $T_W = 294.44$ K, and the Reynolds number is $Re = 1.835 \times 10^5$ with cylinder radius and the far field flow parameters. This test case is taken from the experiment done by Wieting [38]. A non-uniform mesh of 60×160 cells is used with the near-wall cell width of $1/2000$ to resolve the boundary layer. The

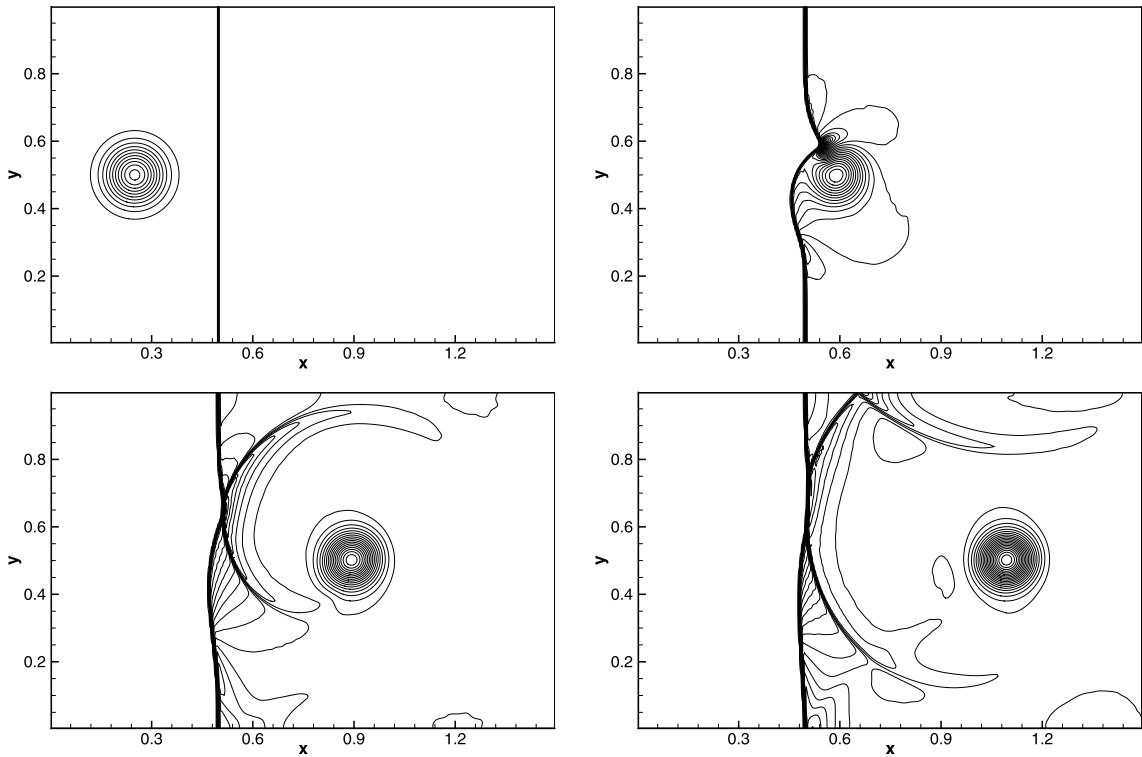


Fig. 7. Shock vortex interaction: the pressure distribution at $t = 0, 0.3, 0.6$ and 0.8 with mesh size $\Delta x = \Delta y = 1/200$.

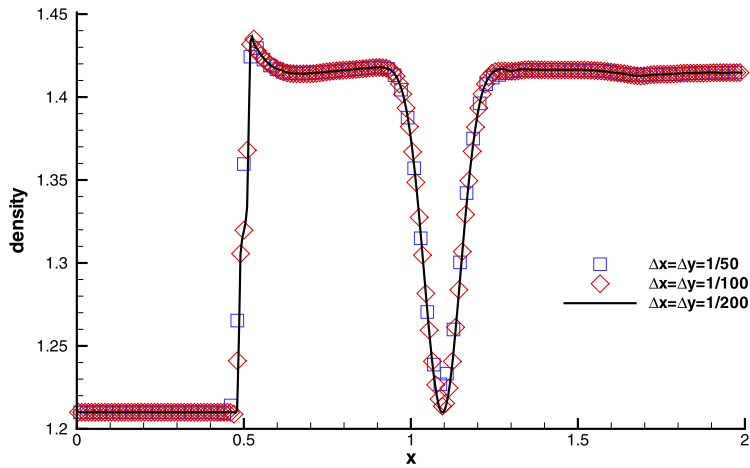


Fig. 8. Shock vortex interaction: the density distribution at $t = 0.8$ along the horizontal symmetric line $y = 0.5$ with mesh size $\Delta x = \Delta y = 1/50, 1/100$ and $1/200$.

mesh, pressure, temperature, and Mach number distributions are given in Fig. 12. The pressure and heat flux along the cylindrical surface are presented in Fig. 13, where the numerical results agree well with the experimental data [38].

4.7. Laminar boundary layer

A laminar boundary layer is tested over a flat plate. The Mach number of the free-stream is $Ma = 0.15$ and the Reynolds number is $Re = U_\infty L/\nu = 10^5$, ν is the viscous coefficient. The non-slip adiabatic boundary condition at the plate is used and a symmetric condition is imposed at the bottom boundary before the flat plate. The non-reflecting boundary condition based on the Riemann invariants is adopted for the other boundaries. A uniform mesh 260×90 points is adopted with $\Delta x = \Delta y = 1/200$, including 60×90 mesh points before the plate. At steady state, the non-dimensional U and V velocity at different locations are presented in Fig. 14, as well as the wall friction coefficient. In all locations, the numerical solutions

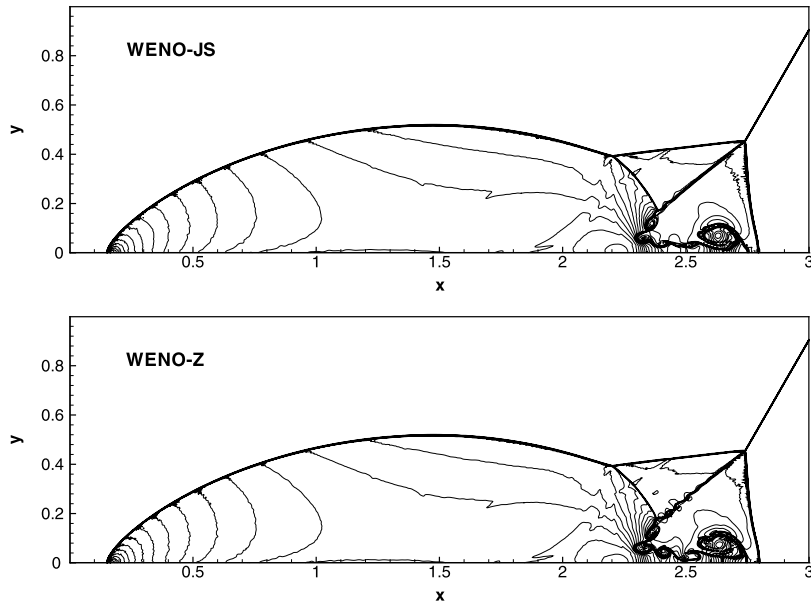


Fig. 9. Double Mach reflection: density contours from WENO-JS and WENO-Z reconstructions with 1440×480 mesh points.

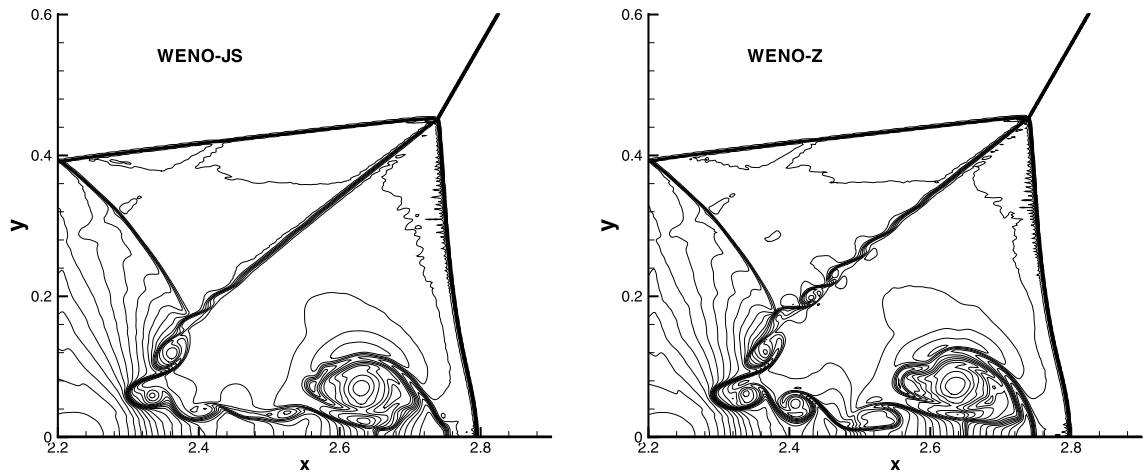


Fig. 10. Double Mach reflection: enlarged density distributions around the triple point with WENO-JS and WENO-Z reconstructions with 1440×480 mesh points.

match with the exact Blasius solution very well. At the upstream location, the boundary layer profile can be accurately captured with only four grid points within the layer.

4.8. Lid-driven cavity flow

In order to further test the scheme in the capturing of vortex flow, the lid-driven cavity problem is one of the most important benchmarks for validating incompressible low speed Navier–Stokes flow solvers. The fluid is bounded by a unit square and is driven by a uniform translation of the top boundary. In this case, the flow is simulated with Mach number $Ma = 0.15$ and all boundaries are isothermal and nonslip. The computational domain $[0, 1] \times [0, 1]$ is covered with 65×65 mesh points. Numerical simulations are conducted for two different Reynolds numbers, i.e., $Re = 1000$ and 3200 . The streamlines in Fig. 15, the U -velocities along the center vertical line, and V -velocities along the center horizontal line, are shown in Fig. 16. The benchmark data [10] for $Re = 1000$ and 3200 are also presented, and the simulation results match well with these benchmark data. The higher-order accuracy of the scheme is clearly demonstrated from the Reynolds number 3200 case, where only 65 uniform mesh points are used in each direction. For such a coarse mesh, the Lattice Boltzmann Method (LBM) will break down easily in the computation [37].

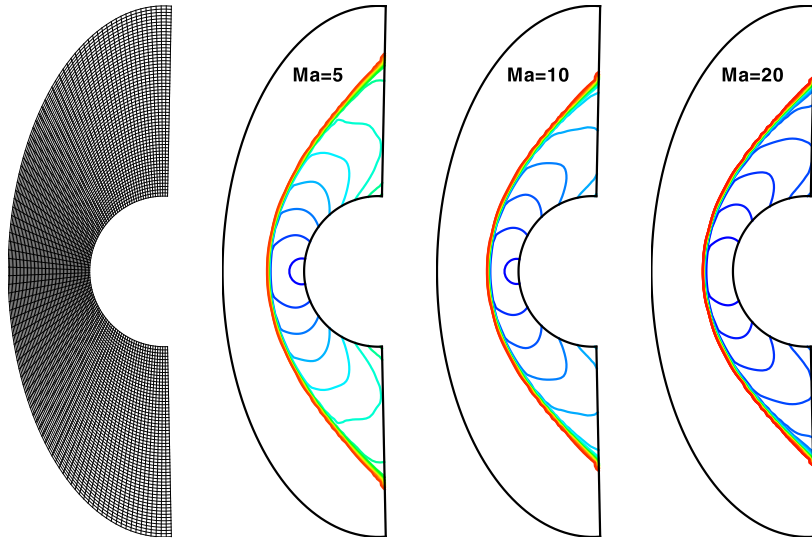


Fig. 11. Hypersonic inviscid flow past a cylinder: the Mach number distributions for the flow with Mach number $Ma = 5, 10$ and 20 .

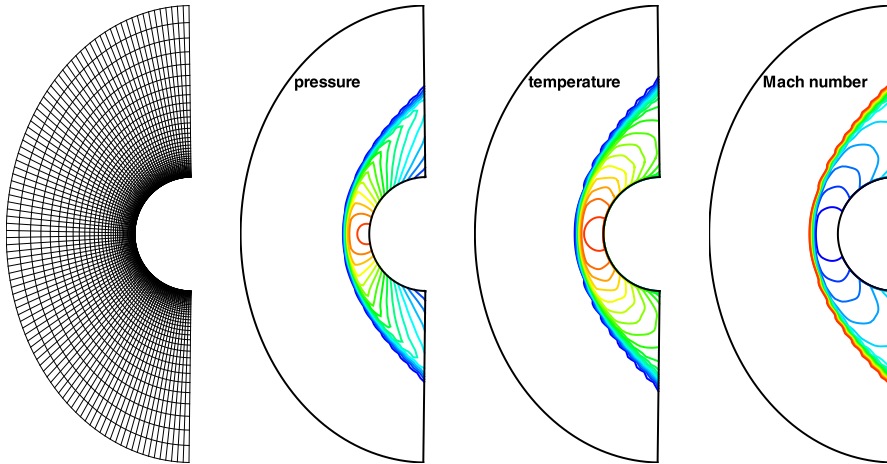


Fig. 12. Hypersonic viscous flow past a cylinder with $Ma = 8.03$: the mesh, pressure, temperature, and Mach number distributions.

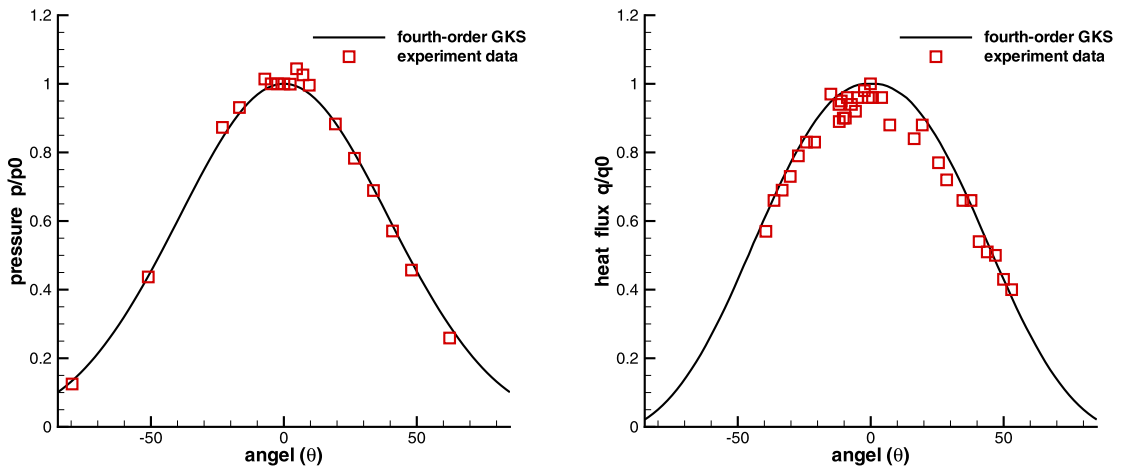


Fig. 13. Hypersonic viscous flow past a cylinder with $Ma = 8.03$. Comparison of the computed pressure and heat flux along the cylindrical surface with the experimental data [38].

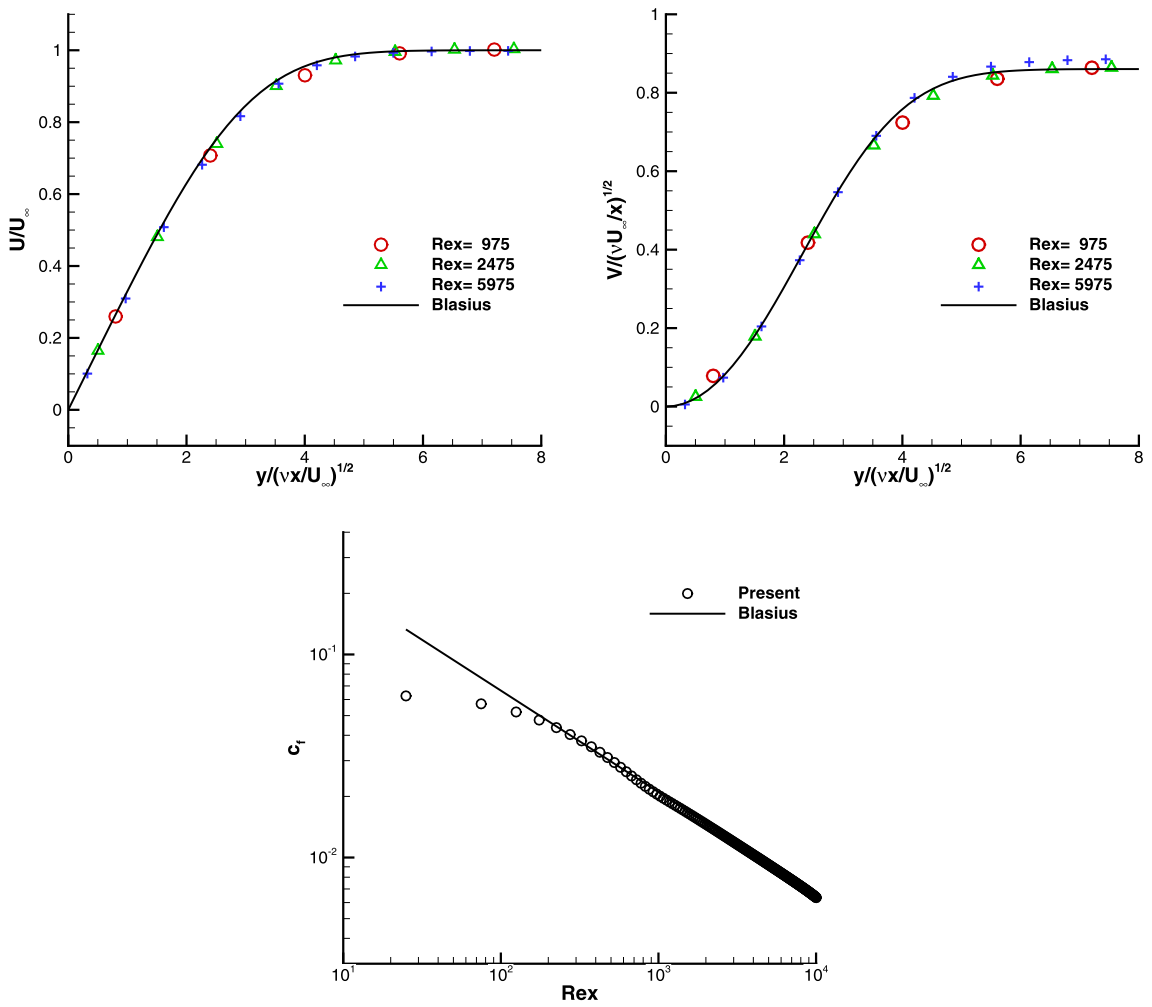


Fig. 14. Laminar boundary layer computation with uniform mesh: the U and V velocity profiles at different locations and wall friction coefficient distribution.

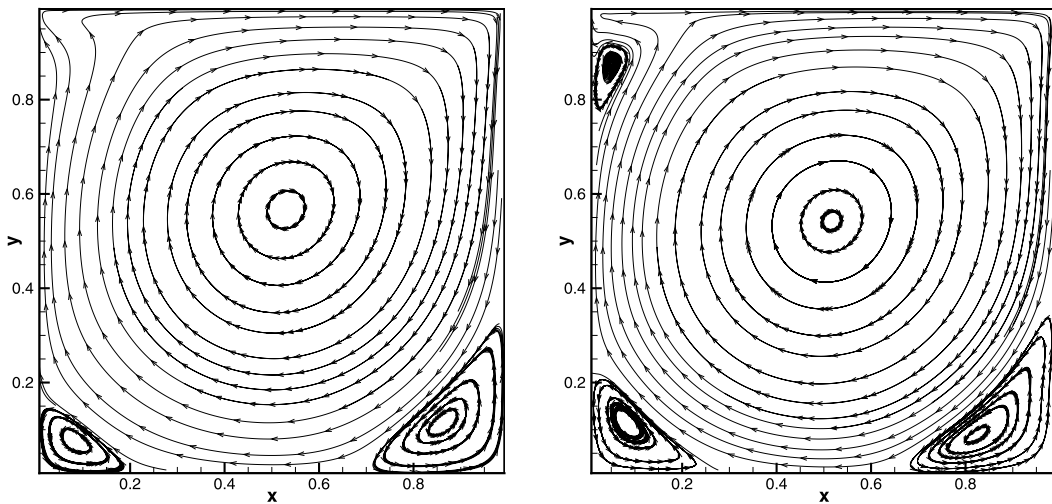


Fig. 15. Lid-driven cavity flow: the streamlines with 65×65 mesh points from the fourth-order GKS at $Re = 1000$ (left) and 3200 (right).

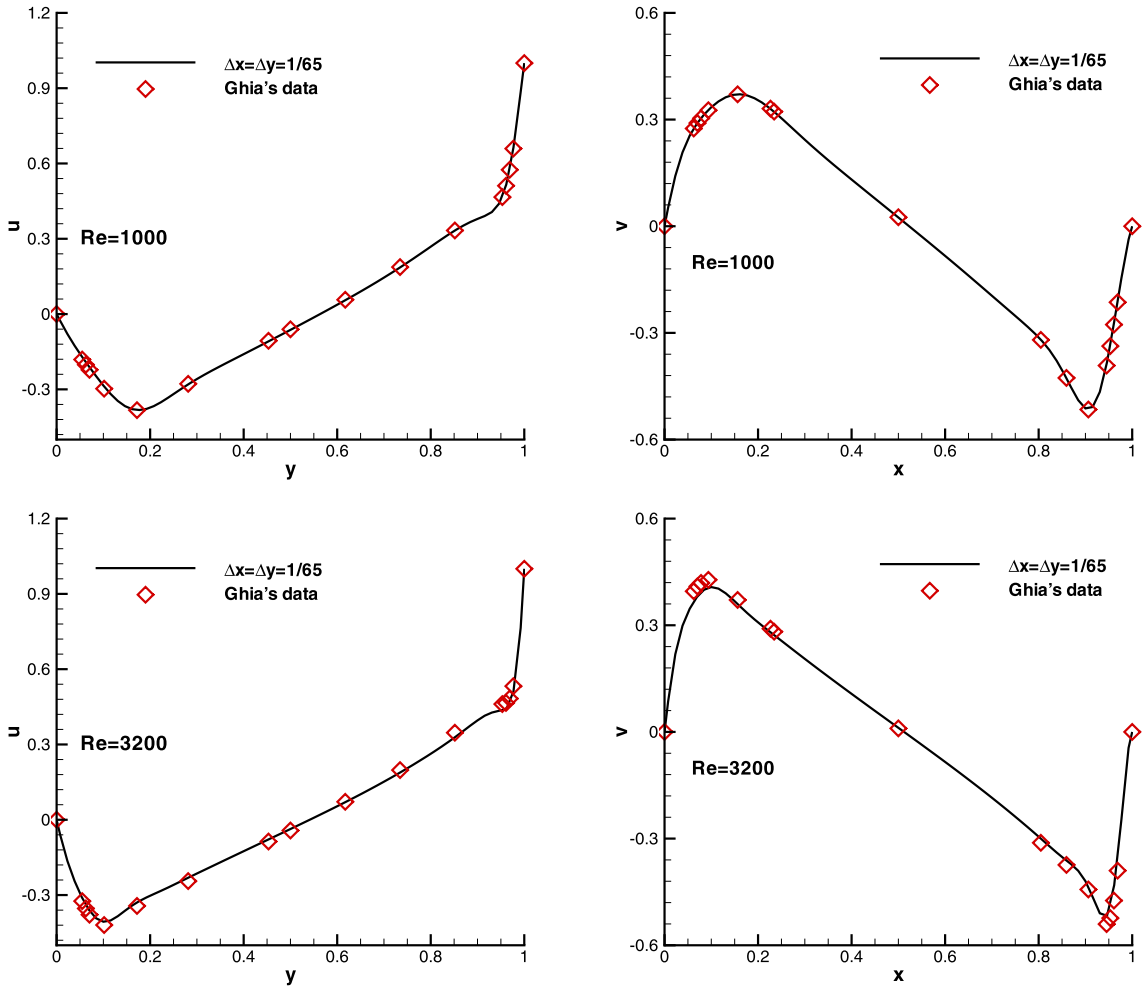


Fig. 16. Lid-driven cavity flow: U -velocity along vertical centerline line and V -velocity along horizontal centerline with 65 mesh points in each direction from the fourth-order GKS at $Re = 1000$ and 3200 .

Table 6
 Comparison of the heights of primary vortex among gas kinetic scheme and other reference methods [17] for the reflecting shock-boundary layer interaction with $\Delta x = \Delta y = 1/500$.

Scheme	AUSMPW+	M-AUSMPW+	Fourth-order GKS
Height	0.163	0.168	0.171

4.9. Viscous shock tube problems

This problem was introduced to test the performance of different schemes for viscous flows [8]. In this case, an ideal gas is at rest in a two-dimensional unit box $[0, 1] \times [0, 1]$. A membrane located at $x = 0.5$ separates two different states of the gas and the dimensionless initial states are

$$(\rho, U, p) = \begin{cases} (120, 0, 120/\gamma), & 0 < x < 0.5, \\ (1.2, 0, 1.2/\gamma), & 0.5 < x < 1, \end{cases}$$

where $\gamma = 1.4$ and Prandtl number $Pr = 0.73$.

The membrane is removed at time zero and wave interaction occurs. A shock wave, followed by a contact discontinuity, moves to the right with Mach number $Ma = 2.37$ and reflects at the right end wall. After the reflection, it interacts with the contact discontinuity. The contact discontinuity and shock wave interact with the horizontal wall and create a thin boundary layer during their propagation. The solution will develop complex two-dimensional shock/shear/boundary-layer interactions. This case is tested in the computational domain $[0, 1] \times [0, 0.5]$, a symmetric boundary condition is used on

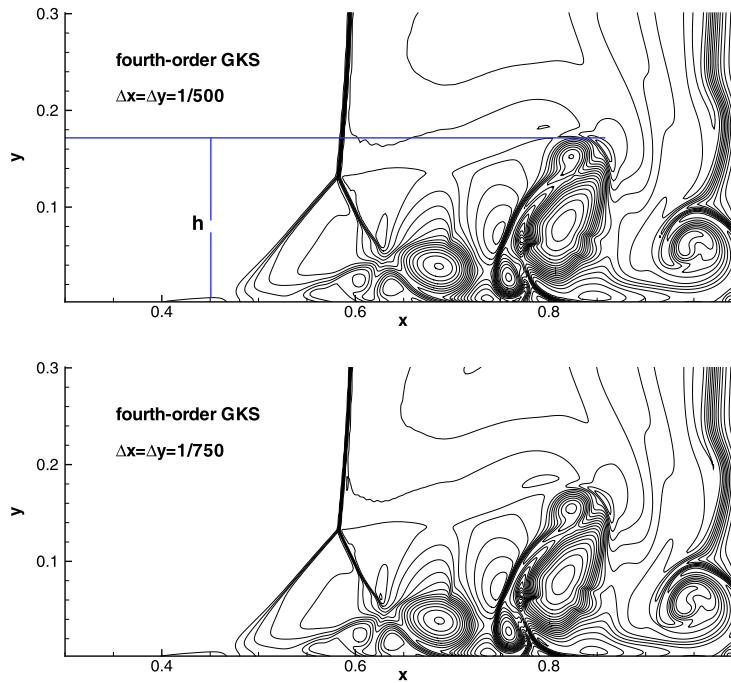


Fig. 17. Reflecting shock-boundary layer interaction: density distributions at $t = 1$ with $Re = 200$ from the fourth-order GKS with $\Delta x = \Delta y = 1/500, 1/750$.

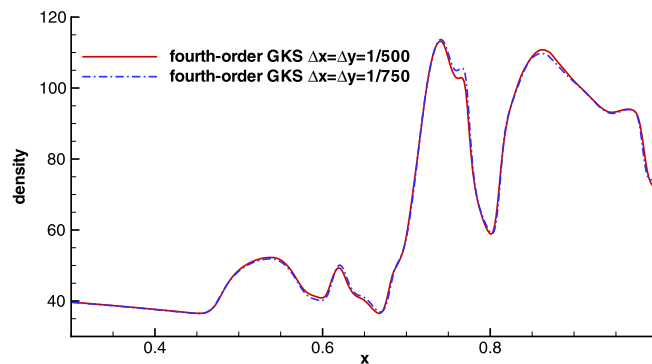


Fig. 18. Reflecting shock-boundary layer interaction: density distribution along the lower wall with different mesh sizes for $Re = 200$.

the top boundary $x \in [0, 1], y = 0.5$. Non-slip adiabatic boundary condition is imposed at solid wall boundaries. The case for $Re = 200$ is tested first. The density distributions are presented in Fig. 17 with two different mesh resolutions. The results match well with each other. The density profiles along the lower wall for $Re = 200$ are also presented in Fig. 18. A mesh-convergent solution is observed for $Re = 200$. As shown in Table 6, the height of primary vortex predicted by the current scheme agrees well with the reference data [17]. For the case with $Re = 1000$, the flow structure becomes more complicated. The density distributions from the current scheme are given in Fig. 19, and the density profiles along the lower wall are presented in Fig. 20 with mesh size $\Delta x = \Delta y = 1/1500$ and $1/2000$. The flow structure is complicated, and the mesh convergence is basically obtained with the mesh size decreasing to $1/1500$. The current results agree well with the reference data. More studies for this problem can be found in [8].

The above test case is for the laminar Navier–Stokes solution only. The calculation is basically the direct numerical simulation. In engineering applications, to model and capture the turbulent flow is still a difficult problem for CFD, especially for the study of turbulent transition [20,46]. For the gas-kinetic scheme, the conventional approach for turbulent flow computation is to determine the turbulent viscosity coefficient from the well-established turbulent modeling equations, and to use this coefficient in the determination of local particle collision time [25,16,34].

5. Conclusion

In this paper, based on the two-stage time stepping method a fourth-order gas-kinetic scheme is proposed for both inviscid and viscous flow computations. With the fifth-order WENO reconstruction, a GKS with a fifth order accuracy in space

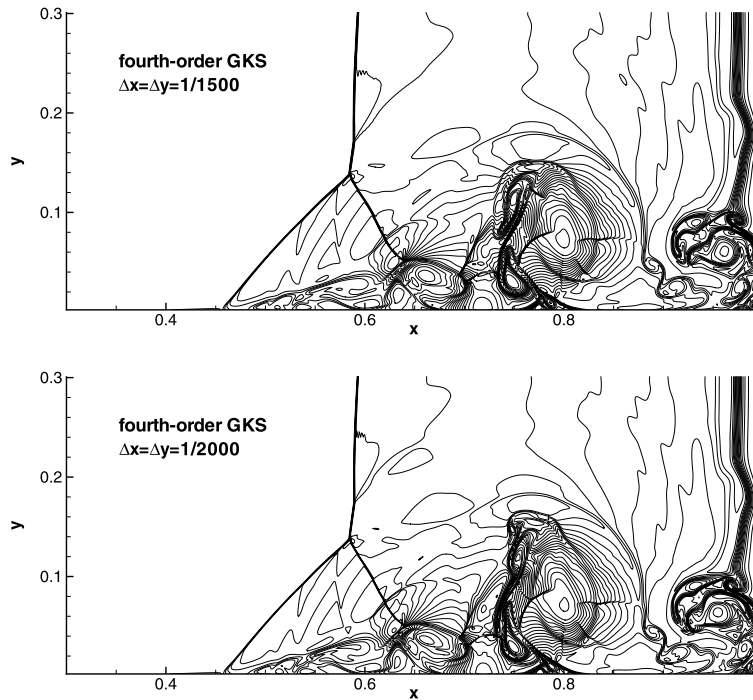


Fig. 19. Reflecting shock-boundary layer interaction. The density distribution at $t = 1$ with $Re = 1000$ with $\Delta x = \Delta y = 1/1500$ and $1/2000$.

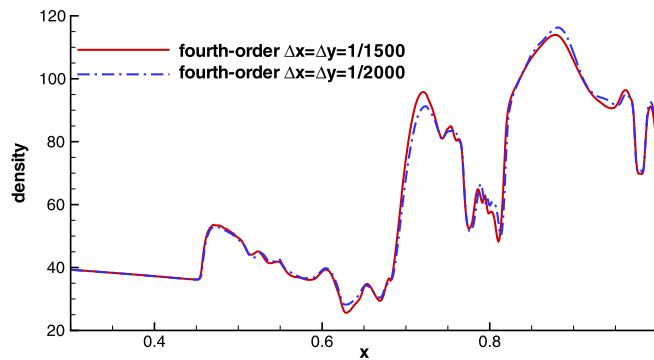


Fig. 20. Reflecting shock-boundary layer interaction: density distribution along the lower wall with different mesh sizes for $Re = 1000$.

and a fourth order accuracy in time, i.e., $\mathcal{O}((\Delta x)^5, (\Delta t)^4)$, is constructed for the Euler equations. For the NS solution, the order of accuracy in time also depends on the particle collision time τ , and the best result obtained is $\mathcal{O}((\Delta x)^5, \tau^2(\Delta t))$. The conventional Runge–Kutta method for the fourth-order accuracy in time needs four stages instead of two in the current method. Therefore, the current GKS should be much more efficient than these higher-order methods based on the standard Runge–Kutta technique, because the higher-order WENO reconstruction takes much more computational time than the evaluation of the flux function. The possible evaluation of the time derivative of the NS flux function in terms of the spatial derivatives in the GKS is due to its underlying physics of hyperbolic transport with local relaxation, where the Cauchy–Kovalevskaya method can be faithfully used. The current finite volume scheme can use a CFL number on the order of 0.5. The further development of the GKS to even higher-order accuracy can be achieved with the inclusion of the second-order time derivative of the flux function, such as the fifth-order scheme presented in the Appendix. Numerically, the order of accuracy of the current scheme has been confirmed. The GKS not only presents accurate solution for the smooth flow, but also has favorable shock capturing property for the discontinuous solution. Most importantly, the numerical tests clearly demonstrate that the current higher-order scheme is as robust as the second-order one.

By taking advantage of the time-accurate gas evolution model in the flux evaluation, an efficient and accurate fourth-order gas-kinetic scheme has been constructed. The advantage of using the time accurate evolution model can be further explored for the construction of higher-order compact schemes [29,30], where the time-dependent gas distribution function at the cell interface not only provides the flux function, but also the conservative flow variables at the next time level for constructing compact stencils in the data reconstruction. Based on the current study, we can conclude that the adapta-

tion of a higher-order gas evolution model for the flux evaluation has an indispensable advantage in the development of higher-order schemes.

Acknowledgements

The authors would like thank referees very much for their great effort in reviewing the manuscript and providing their own detailed analysis of the scheme, which subsequently improve the current method for the NS solutions. The research of K. Xu is supported by Hong Kong Research Grant Council (620813, 16211014, 16207715) and HKUST research fund (PROVOST13SC01, IRS15SC29, SBI14SC11). The research of Q. Li is supported by NSFC (11172154). The work of J. Li is supported by NSFC (91130021, 11371063), the doctoral program from the Ministry of Education of the People's Republic of China (20130003110004), and the Science Challenge Program in China Academy of Engineering Physics.

Appendix A. Extension to higher order

The key point for developing a two-stage fourth-order temporal accurate scheme is the use of a time-dependent flux function. The third-order GRP and GKS have both first- and second-order time derivatives in the flux function [32,24,28,29]. Thus, with a two-stage temporal discretization and the third-order GRP and GKS flux solvers, it is possible to develop a scheme with fifth-order accuracy in time.

We consider the time-dependent equation Eq. (1) with the initial condition Eq. (2). Introducing an intermediate state at $t_* = t_n + A\Delta t$,

$$\mathbf{w}^* = \mathbf{w}^n + A\Delta t\mathcal{L}(\mathbf{w}^n) + \frac{1}{2}A^2\Delta t^2\frac{\partial}{\partial t}\mathcal{L}(\mathbf{w}^n). \quad (23)$$

We can calculate $\mathcal{L}(\mathbf{w}^*)$, $\frac{\partial}{\partial t}\mathcal{L}(\mathbf{w}^*)$ and $\frac{\partial^2}{\partial t^2}\mathcal{L}(\mathbf{w}^*)$ at the intermediate state. Then, the update scheme can be written in a general form,

$$\begin{aligned} \mathbf{w}^{n+1} = \mathbf{w}^n + \Delta t(B_0\mathcal{L}(\mathbf{w}^n) + B_1\mathcal{L}(\mathbf{w}^*)) + \frac{1}{2}\Delta t^2(C_0\frac{\partial}{\partial t}\mathcal{L}(\mathbf{w}^n) + C_1\frac{\partial}{\partial t}\mathcal{L}(\mathbf{w}^*)) \\ + \frac{1}{6}\Delta t^3(D_0\frac{\partial^2}{\partial t^2}\mathcal{L}(\mathbf{w}^n) + D_1\frac{\partial^2}{\partial t^2}\mathcal{L}(\mathbf{w}^*)). \end{aligned} \quad (24)$$

It can be proved that Eq. (23) and Eq. (24) can provide a fifth-order temporal accurate approximation to the solution $\mathbf{w}(t)$ at $t = t_n + \Delta t$ with the following coefficients

$$A = \frac{2}{5}, B_0 = 1, B_1 = 0, C_0 = 1, C_1 = 0, D_0 = \frac{3}{8}, D_1 = \frac{5}{8}. \quad (25)$$

To prove this proposition, the following equation needs to be satisfied, using the same approach as that in [21],

$$\mathbf{w}^{n+1} = \mathbf{w}^n + \int_{t_n}^{t_n+\Delta t} \mathcal{L}(\mathbf{w}(t))dt + \mathcal{O}(\Delta t^6).$$

According to the Taylor expansion of the operator \mathcal{L} at t_n , the integral can be expressed as

$$\int_{t_n}^{t_n+\Delta t} \mathcal{L}(\mathbf{w}(t))dt = \Delta t\mathcal{L} + \frac{\Delta t^2}{2}\frac{\partial\mathcal{L}}{\partial t} + \frac{\Delta t^3}{6}\frac{\partial^2\mathcal{L}}{\partial t^2} + \frac{\Delta t^4}{24}\frac{\partial^3\mathcal{L}}{\partial t^3} + \frac{\Delta t^5}{120}\frac{\partial^4\mathcal{L}}{\partial t^4} + \mathcal{O}(\Delta t^6), \quad (26)$$

where the time derivatives for the operator \mathcal{L} can be given with the chain rule as follows,

$$\begin{aligned} \mathcal{L}_t &= \mathcal{L}_w\mathcal{L}, \\ \mathcal{L}_{tt} &= \mathcal{L}_w^2\mathcal{L} + \mathcal{L}_{ww}\mathcal{L}^2, \\ \mathcal{L}_{ttt} &= \mathcal{L}_w^3\mathcal{L} + 4\mathcal{L}_{ww}\mathcal{L}_w\mathcal{L}^2 + \mathcal{L}_{www}\mathcal{L}^3, \\ \mathcal{L}_{tttt} &= \mathcal{L}_w^4\mathcal{L} + 4\mathcal{L}_{ww}^2\mathcal{L}^3 + 11\mathcal{L}_{ww}\mathcal{L}_w^2\mathcal{L}^2 + 7\mathcal{L}_{www}\mathcal{L}_w\mathcal{L}^3 + \mathcal{L}_{wwww}\mathcal{L}^4. \end{aligned}$$

Denote $\mathcal{G}(\mathbf{w}) = \frac{\partial}{\partial t}\mathcal{L}(\mathbf{w})$ and $\mathcal{H}(\mathbf{w}) = \frac{\partial^2}{\partial t^2}\mathcal{L}(\mathbf{w})$. With the chain rule and the definition of the operator, the derivatives for operators \mathcal{G} and \mathcal{H} are written as

$$\begin{aligned} \mathcal{G}_w &= \mathcal{L}_{ww}\mathcal{L} + \mathcal{L}_w^2, \\ \mathcal{G}_{ww} &= \mathcal{L}_{www}\mathcal{L} + 3\mathcal{L}_{ww}\mathcal{L}_w, \\ \mathcal{G}_{www} &= \mathcal{L}_{wwww}\mathcal{L} + 4\mathcal{L}_{www}\mathcal{L}_w + 3\mathcal{L}_{ww}^2, \\ \mathcal{H}_w &= \mathcal{L}_{www}\mathcal{L}^2 + 4\mathcal{L}_{ww}\mathcal{L}_w\mathcal{L} + \mathcal{L}_w^3, \\ \mathcal{H}_{ww} &= \mathcal{L}_{wwww}\mathcal{L}^2 + 6\mathcal{L}_{www}\mathcal{L}_w\mathcal{L} + 7\mathcal{L}_{ww}\mathcal{L}_w^2 + 4\mathcal{L}_{ww}^2\mathcal{L}. \end{aligned}$$

According to the definition of the intermediate stage, $\mathcal{L}(\mathbf{w})$, $\mathcal{G}(\mathbf{w})$ and $\mathcal{H}(\mathbf{w})$ in the neighboring of \mathbf{w}^* up to the corresponding order, we have

$$\begin{aligned} \mathcal{L}(\mathbf{w}^*) &= \mathcal{L}(\mathbf{w}^n) + \mathcal{L}_w(\mathbf{w}^* - \mathbf{w}^n) + \frac{\mathcal{L}_{ww}}{2}(\mathbf{w}^* - \mathbf{w}^n)^2 + \frac{\mathcal{L}_{www}}{6}(\mathbf{w}^* - \mathbf{w}^n)^3 + \frac{\mathcal{L}_{wwww}}{24}(\mathbf{w}^* - \mathbf{w}^n)^4, \\ \mathcal{G}(\mathbf{w}^*) &= \mathcal{G}(\mathbf{w}^n) + \mathcal{G}_w(\mathbf{w}^* - \mathbf{w}^n) + \frac{\mathcal{G}_{ww}}{2}(\mathbf{w}^* - \mathbf{w}^n)^2 + \frac{\mathcal{G}_{www}}{6}(\mathbf{w}^* - \mathbf{w}^n)^3, \\ \mathcal{H}(\mathbf{w}^*) &= \mathcal{H}(\mathbf{w}^n) + \mathcal{H}_w(\mathbf{w}^* - \mathbf{w}^n) + \frac{\mathcal{H}_{ww}}{2}(\mathbf{w}^* - \mathbf{w}^n)^2, \end{aligned}$$

where higher order terms are ignored, and \mathbf{w}^* is given by Eq. (23). Substituting $\mathcal{L}(\mathbf{w}^*)$, $\mathcal{G}(\mathbf{w}^*)$, $\mathcal{H}(\mathbf{w}^*)$ into Eq. (24) and collecting the terms of the same order, we obtain

$$\begin{aligned} (\mathbf{w}^{n+1} - \mathbf{w}^n) &= \Delta t(B_0 + B_1)\mathcal{L} + \frac{\Delta t^2}{2}(C_0 + C_1 + 2B_1A)\mathcal{L}_w\mathcal{L} \\ &+ \frac{\Delta t^3}{6}(D_0 + D_1 + 3B_1A^2 + 3C_1A)(\mathcal{L}_w^2\mathcal{L} + \mathcal{L}_{ww}\mathcal{L}^2) \\ &+ \frac{\Delta t^4}{6}D_1A(\mathcal{L}_{www}\mathcal{L}^3 + 4\mathcal{L}_{ww}\mathcal{L}_w\mathcal{L}^2 + \mathcal{L}_w^3\mathcal{L}) \\ &+ \frac{\Delta t^4}{24}\left[(6C_1A^2)\mathcal{L}_w^3\mathcal{L} + (4B_1A^3 + 6C_1A^2)\mathcal{L}_{www}\mathcal{L}^3 + (12B_1A^3 + 24C_1A^2)\mathcal{L}_{ww}\mathcal{L}_w\mathcal{L}^2\right] \\ &+ \frac{\Delta t^5}{24}(B_1A^4 + 2C_1A^3 + 2D_1A^2)\mathcal{L}_{wwww}\mathcal{L}^4 \\ &+ \frac{\Delta t^5}{24}(6B_1A^4 + 14C_1A^3 + 14D_1A^2)\mathcal{L}_{www}\mathcal{L}_w\mathcal{L}^3 \\ &+ \frac{\Delta t^5}{24}(3B_1A^4 + 18C_1A^3 + 22D_1A^2)\mathcal{L}_{ww}\mathcal{L}_w^2\mathcal{L}^2 \\ &+ \frac{\Delta t^5}{24}(6C_1A^3 + 8D_1A^2)\mathcal{L}_{ww}^2\mathcal{L}^3 \\ &+ \frac{\Delta t^5}{24}(2D_1A^2)\mathcal{L}_w^4\mathcal{L}. \end{aligned}$$

Comparing the above coefficients with Eq. (26), we have

$$\begin{aligned} B_0 &= 1, B_1 = 0, C_0 = 1, C_1 = 0, \\ D_0 + D_1 &= 1, D_1A = \frac{1}{4}, D_1A^2 = \frac{1}{10}. \end{aligned}$$

Solving the above equations yields all coefficients in Eq. (25). We emphasize that this set of coefficients is unique, which provides a unique two-stage approach for a fifth-order accuracy.

In order to develop the gas-kinetic scheme with fifth-order temporal accuracy, the time-dependent flux should be approximated by the quadratic function, which is expressed as follows

$$F_{i+1/2}(W^n, t) = F_{i+1/2}^n + \partial_t F_{i+1/2}^n t + \frac{1}{2} \partial_{tt} F_{i+1/2}^n t^2. \tag{27}$$

Within a time step, the coefficients $F_{i+1/2}^n$, $\partial_t F_{i+1/2}^n$ and $\partial_{tt} F_{i+1/2}^n$ can be determined by imposing the conditions

$$\begin{aligned} F_{i+1/2}\Delta t + \frac{1}{2}\partial_t F_{i+1/2}\Delta t^2 + \frac{1}{6}\partial_{tt} F_{i+1/2}\Delta t^3 &= \mathbb{F}_{i+1/2}(W^n, \Delta t), \\ \frac{2}{3}F_{i+1/2}\Delta t + \frac{2}{9}\partial_t F_{i+1/2}\Delta t^2 + \frac{4}{81}\partial_{tt} F_{i+1/2}\Delta t^3 &= \mathbb{F}_{i+1/2}(W^n, 2\Delta t/3), \\ \frac{1}{3}F_{i+1/2}\Delta t + \frac{1}{18}\partial_t F_{i+1/2}\Delta t^2 + \frac{1}{162}\partial_{tt} F_{i+1/2}\Delta t^3 &= \mathbb{F}_{i+1/2}(W^n, \Delta t/3), \end{aligned}$$

where

$$\mathbb{F}_{i+1/2}(W^n, \delta) = \int_{t_n}^{t_n+\delta} \int u \psi f(x_{i+1/2}, t, u, v, \xi) d\xi dt.$$

The formulation for the gas distribution $f(x_{i+1/2}, t, u, v, \xi)$ can be found in [24,28,29]. By solving the linear system, all coefficients can be determined as follows

$$\begin{aligned} F_{i+1/2}(W^n, t_n) &= (\mathbb{F}_{i+1/2}(W^n, \Delta t) - 4.5\mathbb{F}_{i+1/2}(W^n, 2\Delta t/3) + 9\mathbb{F}_{i+1/2}(W^n, \Delta t/3))/\Delta t, \\ \partial_t F_{i+1/2}(W^n, t_n) &= -9(\mathbb{F}_{i+1/2}(W^n, \Delta t) - 4\mathbb{F}_{i+1/2}(W^n, 2\Delta t/3) + 5\mathbb{F}_{i+1/2}(W^n, \Delta t/3))/\Delta t^2, \\ \partial_{tt} F_{i+1/2}(W^n, t_n) &= 9(3\mathbb{F}_{i+1/2}(W^n, \Delta t) - 9\mathbb{F}_{i+1/2}(W^n, 2\Delta t/3) + 9\mathbb{F}_{i+1/2}(W^n, \Delta t/3))/\Delta t^3. \end{aligned}$$

In smooth flow regions, with the fifth-order WENO reconstruction the above scheme solves the Euler equations with the error on the order $\mathcal{O}((\Delta x)^5, (\Delta t)^5)$, and the NS equations with $\mathcal{O}((\Delta x)^5, \tau^2 \Delta t, \tau(\Delta t)^2)$.

References

- [1] M. Ben-Artzi, J. Falcovitz, A second-order Godunov-type scheme for compressible fluid dynamics, *J. Comput. Phys.* 55 (1984) 1–32.
- [2] M. Ben-Artzi, J. Li, G. Warnecke, A direct Eulerian GRP scheme for compressible fluid flows, *J. Comput. Phys.* 218 (2006) 19–43.
- [3] M. Ben-Artzi, J. Li, Hyperbolic conservation laws: Riemann invariants and the generalized Riemann problem, *Numer. Math.* 106 (2007) 369–425.
- [4] P.L. Bhatnagar, E.P. Gross, M. Krook, A model for collision processes in gases, I: small amplitude processes in charged and neutral one-component systems, *Phys. Rev.* 94 (1954) 511–525.
- [5] M. Castro, B. Costa, W.S. Don, High order weighted essentially non-oscillatory WENO-Z schemes for hyperbolic conservation laws, *J. Comput. Phys.* 230 (2011) 1766–1792.
- [6] S. Chapman, T.G. Cowling, *The Mathematical Theory of Non-Uniform Gases*, third edition, Cambridge University Press, 1990.
- [7] B. Cockburn, C.W. Shu, Runge–Kutta discontinuous Galerkin methods for convection-dominated problems, *J. Sci. Comput.* 16 (2001) 173–261.
- [8] V. Daru, C. Tenaud, Numerical simulation of the viscous shock tube problem by using a high resolution monotonicity-preserving scheme, *Comput. Fluids* 38 (2009) 664–676.
- [9] M. Dumbser, D.S. Balsara, E.F. Toro, C.D. Munz, A unified framework for the construction of one-step finite volume and discontinuous Galerkin schemes on unstructured meshes, *J. Comput. Phys.* 227 (2008) 8209–8253.
- [10] U. Ghia, K.N. Ghia, C.T. Shin, High-Re solutions for incompressible flow using the Navier–Stokes equations and a multigrid method, *J. Comput. Phys.* 48 (1982) 387–411.
- [11] S. Gottlieb, C.W. Shu, Total variation diminishing Runge–Kutta schemes, *Math. Comput.* 67 (1998) 73–85.
- [12] E. Han, J. Li, H. Tang, Accuracy of the adaptive GRP scheme and the simulation of 2-D Riemann problem for compressible Euler equations, *Commun. Comput. Phys.* 10 (2011) 577–606.
- [13] A. Harten, B. Engquist, S. Osher, S.R. Chakravarthy, Uniformly high order accurate essentially non-oscillatory schemes, III, *J. Comput. Phys.* 71 (1987) 231–303.
- [14] S. Li, F. Xiao, High order multi-moment constrained finite volume method, part I: basic formulation, *J. Comput. Phys.* 228 (2009) 3669–3707.
- [15] G.S. Jiang, C.W. Shu, Efficient implementation of weighted ENO schemes, *J. Comput. Phys.* 126 (1996) 202–228.
- [16] J. Jiang, Y.H. Qian, Implicit gas-kinetic BGK scheme with multigrid for 3D stationary transonic high-Reynolds number flows, *Comput. Fluids* 66 (2012) 21–28.
- [17] K.H. Kim, C. Kim, Accurate, efficient and monotonic numerical methods for multi-dimensional compressible flows, part I: spatial discretization, *J. Comput. Phys.* 208 (2005) 527–569.
- [18] G. Kumar, S.S. Girimaji, J. Kerimo, WENO-enhanced gas-kinetic scheme for direct simulations of compressible transition and turbulence, *J. Comput. Phys.* 234 (2013) 499–523.
- [19] P.D. Lax, X.D. Liu, Solution of two-dimensional Riemann problems of gas dynamics by positive schemes, *SIAM J. Sci. Comput.* 19 (1998) 319–340.
- [20] C.B. Lee, J.Z. Wu, Transition in wall-bounded flows, *Appl. Mech. Rev.* 61 (3) (2008) 802.
- [21] J. Li, Z. Du, A two-stage fourth order time-accurate discretization for Lax–Wendroff type flow solvers, I: hyperbolic conservation laws, *SIAM J. Sci. Comput.* (2016), in press.
- [22] J. Li, Q. Li, K. Xu, Comparison of the generalized Riemann solver and the gas-kinetic scheme for inviscid compressible flow simulations, *J. Comput. Phys.* 230 (2011) 5080–5099.
- [23] J. Li, T. Zhang, S. Yang, *The two-dimensional Riemann problem in gas dynamics*, Pitman Monographs and Surveys in Pure and Applied Mathematics, vol. 98, Longman Scientific & Technical, Harlow, 1998.
- [24] Q.B. Li, K. Xu, S. Fu, A high-order gas-kinetic Navier–Stokes flow solver, *J. Comput. Phys.* 229 (2010) 6715–6731.
- [25] Q.B. Li, S. Tan, S. Fu, K. Xu, Numerical simulation of compressible turbulence with gas-kinetic BGK scheme, in: *Proceedings of the 13th Asian Congress of Fluid Mechanics*, Dhaka, Bangladesh, 12–21 December, 2010, pp. 12–21.
- [26] N. Liu, H.Z. Tang, A high-order accurate gas-kinetic scheme for one- and two-dimensional flow simulation, *Commun. Comput. Phys.* 15 (2014) 911–943.
- [27] X.D. Liu, S. Osher, T. Chan, Weighted essentially non-oscillatory schemes, *J. Comput. Phys.* 115 (1994) 200–212.
- [28] J. Luo, K. Xu, A high-order multidimensional gas-kinetic scheme for hydrodynamic equations, *Sci. China, Technol. Sci.* 56 (2013) 2370–2384.
- [29] L. Pan, K. Xu, A compact third-order gas-kinetic scheme for compressible Euler and Navier–Stokes equations, *Commun. Comput. Phys.* 18 (2015) 985–1011.
- [30] L. Pan, K. Xu, A third-order compact gas-kinetic scheme on unstructured meshes for compressible Navier–Stokes solutions, *J. Comput. Phys.* 318 (2016) 327–348.
- [31] M. Pandolfi, D. D’Ambrosio, Numerical instabilities in upwind methods: analysis and cures for the “carbuncle” phenomenon, *J. Comput. Phys.* 166 (2001) 271–301.
- [32] J. Qian, J. Li, S. Wang, The generalized Riemann problems for compressible fluid flows: towards high order, *J. Comput. Phys.* 259 (2014) 358–389.
- [33] X. Ren, K. Xu, W. Shyy, C. Gu, A multi-dimensional high-order discontinuous Galerkin method based on gas kinetic theory for viscous flow computations, *J. Comput. Phys.* 292 (2015) 176–193.
- [34] M. Righi, A modified gas-kinetic scheme for turbulent flow, *Commun. Comput. Phys.* 16 (1) (2014) 239–263.
- [35] C.W. Shu, S. Osher, Efficient implementation of essentially nonoscillatory shock-capturing schemes II, *J. Comput. Phys.* 83 (1989) 32–78.

- [36] E. Toro, *Riemann Solvers and Numerical Methods for Fluid Dynamics*, Springer, 1997.
- [37] Peng Wang, Lianhua Zhu, Zhaoli Guo, Kun Xu, A comparative study of LBE and DUGKS methods for nearly incompressible flows, *Commun. Comput. Phys.* 17 (3) (2015) 657–681.
- [38] A.R. Wieting, Experimental study of shock wave interface heating on a cylindrical leading edge, No. NASA TM-100484, 1987.
- [39] P. Woodward, P. Colella, Numerical simulations of two-dimensional fluid flow with strong shocks, *J. Comput. Phys.* 54 (1984) 115–173.
- [40] K. Xu, Super-Burnett solutions for Poiseuille flow, *Phys. Fluids* 15 (2003) 2077–2080.
- [41] K. Xu, *Direct Modeling for Computational Fluid Dynamics: Construction and Application of Unified Gas Kinetic Schemes*, World Scientific, 2015.
- [42] K. Xu, A gas-kinetic BGK scheme for the Navier–Stokes equations and its connection with artificial dissipation and Godunov method, *J. Comput. Phys.* 171 (2001) 289–335.
- [43] K. Xu, J.C. Huang, A unified gas-kinetic scheme for continuum and rarefied flows, *J. Comput. Phys.* 229 (2010) 7747–7764.
- [44] K. Xu, Z.H. Li, Microchannel flow in the slip regime: gas-kinetic BGK–Burnett solutions, *J. Fluid Mech.* 513 (2004) 87–110.
- [45] K. Xu, M.L. Mao, L. Tang, A multidimensional gas-kinetic BGK scheme for hypersonic viscous flow, *J. Comput. Phys.* 203 (2005) 405–421.
- [46] C.H. Zhang, et al., Transition in hypersonic boundary layers, *AIP Adv.* 5 (2015) 107137.